



## 저작자표시-비영리-변경금지 2.0 대한민국

이용자는 아래의 조건을 따르는 경우에 한하여 자유롭게

- 이 저작물을 복제, 배포, 전송, 전시, 공연 및 방송할 수 있습니다.

다음과 같은 조건을 따라야 합니다:



저작자표시. 귀하는 원저작자를 표시하여야 합니다.



비영리. 귀하는 이 저작물을 영리 목적으로 이용할 수 없습니다.



변경금지. 귀하는 이 저작물을 개작, 변형 또는 가공할 수 없습니다.

- 귀하는, 이 저작물의 재이용이나 배포의 경우, 이 저작물에 적용된 이용허락조건을 명확하게 나타내어야 합니다.
- 저작권자로부터 별도의 허가를 받으면 이러한 조건들은 적용되지 않습니다.

저작권법에 따른 이용자의 권리는 위의 내용에 의하여 영향을 받지 않습니다.

이것은 [이용허락규약\(Legal Code\)](#)을 이해하기 쉽게 요약한 것입니다.

[Disclaimer](#)

공학박사 학위논문

**Studies on Nickel Oxide as  
Hole Transporting Material for  
High Performance Photovoltaics**

니켈 산화물 기반의 정공 전달 물질을 활용한  
고성능 광전자 소자에 관한 연구

2023년 2월

서울대학교 대학원

재료공학부

박 성 진

# Studies on Nickel Oxide as Hole Transporting Material for High Performance Photovoltaics

니켈 산화물 기반의 정공 전달 물질을 활용한  
고성능 광전자 소자에 관한 연구

지도교수 박 수 영

이 논문을 공학박사 학위논문으로 제출함

2023년 2월

서울대학교 대학원

재료공학부

박 성 진

박성진의 박사 학위논문을 인준함

2023년 2월

위 원 장      안   철   희      (인)

부 위 원 장      박   수   영      (인)

위      원      권   민   상      (인)

위      원      김   진   영      (인)

위      원      안   병   관      (인)

# **Abstract**

## **Studies on Nickel Oxide as Hole Transporting Material for High Performance Photovoltaics**

Sungjin Park

Department of Materials Science and Engineering

The Graduate School

Seoul National University

Energy is one of the most important issues in 21<sup>st</sup> century. The growing demand for renewable energy such as solar energy is inevitable in order to impede climate change and prevent climate crisis. Although majority of the commercialized photovoltaic cells are silicon based solar cells, immense amount of research and development are being made for next-generation solar cells such as perovskite solar cells (PSCs) and organic solar cells (OSCs). The performance of these photovoltaic cells are determined not only by the quality of light-absorbing materials but also by the charge transporting materials which selectively transport charges to respective electrodes. Due to the development of innovative materials, the power conversion efficiency (PCE) of these emerging solar cells have risen sharply and have become comparable to that of silicon solar cells. However, these photovoltaic cells still have challenges to overcome before commercialization. This dissertation is focused on development of high performance photovoltaic cells using nickel oxide (NiO) as hole transporting materials (HTMs). The strategy of enhancing both stability and

performance of solar cells is investigated with the use of salt stabilizers. Furthermore, a novel dipole-possessed additive is applied in order to improve charge transport properties of solar cells.

In Chapter 2, virtually neutral ammonium salt stabilizer is presented as a novel stabilizer for NiO. The use of different stabilizers for NiO resulted in different morphological and optoelectronic properties. NiO with salt stabilizer as HTM showed improved hole transport, stronger interaction with perovskite layer and enhanced ambient stability. Based on this novel NiO, highly stable and efficient methylammonium lead iodide (MAPbI<sub>3</sub>) PSC is successfully demonstrated.

In Chapter 3, effective energy level modulation of previously developed NiO was conducted. Hydroquinone sulfonic acid (HSA) salts which possess dipole moment are used as additive for NiO to overcome the energetic barrier between inorganic NiO HTM and organic bulkheterojunction (BHJ) layer. The formation of surface dipole and charge tunneling enhanced hole extraction from the BHJ layer to NiO. OSCs based on this modified NiO exhibited clear increase in open circuit voltage ( $V_{oc}$ ), thereby achieving high performance OSCs based on metal oxide HTM.

**Keywords: Photovoltaics, hole transporting materials, nickel oxide, ammonium salt stabilizers, dipole induced energy level modification**

**Student Number: 2017-28672**

# Contents

<b>Abstracts.....</b>	<b>3</b>
<b>List of Tables .....</b>	<b>7</b>
<b>List of Figures .....</b>	<b>8</b>
<b>Chapter 1. Introduction .....</b>	<b>13</b>
1.1 Overview of photovoltaics .....	13
1.2 Emerging photovoltaics.....	15
1.2.1 Perovskite solar cells .....	18
1.2.2 Organic solar cells .....	19
1.3 Device characterization .....	22
1.3.1 Charge transport .....	23
1.3.2 Charge recombination .....	24
1.4 Charge transporting materials.....	26
1.4.1 Hole transporting materials .....	27
1.4.2 Metal oxide.....	28
1.4.3 Nickel oxide .....	29
1.5 Research objectives and outlines.....	31
1.6 Bibliography.....	34
<b>Chapter 2. Nickel oxide hole transporting material employing ammonium salt stabilizer for high performance perovskite solar cells .....</b>	<b>37</b>
2.1 Research background.....	37
2.2 Experimental methods.....	40
2.2.1 Material preparation .....	40
2.2.2 Perovskite solar cell fabrication .....	40

2.2.3 Characterization .....	41
2.3 Result and Discussions .....	42
2.4 Conclusion and outlook .....	66
2.5 Bibliography .....	67

## **Chapter 3. Nickel oxide utilizing dipole induced energy level modification for high performance non-fullerene organic solar cells..... 72**

3.1 Research background.....	72
3.2 Experimental methods.....	75
3.2.1 Material preparation .....	75
3.2.2 Organic solar cell fabrication .....	75
3.2.3 Characterization .....	76
3.3 Result and Discussions .....	77
3.4 Conclusion and outlook.....	93
3.5 Bibliography .....	94

## **국 문 초 록 (Korean Abstract).....98**

## **List of Publications.....100**

## **List of Presentations.....101**

## **List of Patents .....101**

## List of Tables

Table 2-1. Full width at half maximum (FWHM) of ITO/NiO with different stabilizer conditions at different peaks .....	45
Table 2-2. Calculated $\text{Ni}^{3+} / \text{Ni}^{2+}$ ratio for each NiO films in Ni 2p <sub>3/2</sub> and O 1s orbital. The ratio was calculated by using respective area of deconvoluted peak from XPS data shown in bracket.....	50
Table 2-3. Device parameters of the PSCs based on different HTM. The device parameters of PEDOT:PSS based device are also provided for comparison. Results are extracted from $J-V$ measurements under standard AM 1.5 illumination (100 mW cm <sup>-2</sup> ) .....	54
Table 3-1. Photovoltaic parameters of PM6:Y6-BO-4F OSC devices based on different HTM conditions.....	76
Table 3-2. Thickness of different NiO films on top of SiO <sub>2</sub> substrate using spectroscopic ellipsometry measurements .....	78
Table 3-3. Photovoltaic parameters of optimized OSCs using different HTMs.....	83
Table 3-4. Photovoltaic parameters of PM6:Y6-BO-4F OSC devices using NiO / HSA based salts.....	84
Table 3-5. Photovoltaic parameters of PM6:Y6-BO-4F OSCs based on NiO with different volume ratio of HSA-K and HSA-Na salt .....	85
Table 3-6. Photovoltaic parameters of PCE-10:PC <sub>71</sub> BM OSCs based on different HTMs. ....	89



## List of Figures

Fig. 1-1. Development of CO <sub>2</sub> content in the atmosphere in the last 22,000 years. Noticeable is the steep rise since the start of industrialization .....	14
Fig. 1-2. Distribution of worldwide energy consumption in 2014 .....	14
Fig. 1-3. Different generation photovoltaics .....	16
Fig. 1-4. Best research-cell efficiency chart with highest confirmed conversion efficiencies for different types of cells from 1976 .....	17
Fig. 1-5. a) ABX <sub>3</sub> perovskite crystal structure and b) n-i-p and p-i-n perovskite solar cell architecture and c) perovskite film fabrication process using solution process .....	19
Fig. 1-6. Working principle of organic solar cell and external quantum efficiency. ....	21
Fig. 1-7. The development of organic solar cell with the invention of a) bulkheterojunction and b) non-fullerene acceptors .....	21
Fig. 1-8. <i>J-V</i> characteristic and parameters in solar cells .....	23
Fig. 1-9. Charge transport and recombination mechanisms in solar cells.....	25
Fig. 1-10. Structure of solar cell which is composed of active layer and charge transporting layers .....	26
Fig. 1-11. Band structure of Ni metal and NiO. Cubic rocksalt (NaCl) structure of NiO and absorption coefficient of NiO .....	31
Fig. 1-12. An overview of each chapter of this dissertation.....	33
Fig. 2-1. a) Schematic preparation procedure of NiO solution with different stabilizers and diverse concentration resulting in different NiO solution color. b) Top-view scanning electron microscopy images of NiO films with different stabilizer	

conditions at 100 K magnification. c) Atomic force microscopy images of NiO films with different stabilizer conditions in an area of  $5\ \mu\text{m} \times 5\ \mu\text{m}$ . RMS is the root mean square roughness of the film .....43

Fig. 2-2. a) Reaction of amine and strong acid for formation of ammonium salt. b) Reaction of monoethanolamine and hydrochloric acid.....45

Fig. 2-3. a) Images of NiO solutions for a) P-NiO, b) A-NiO, c) B-NiO, and d) S-NiO.....45

Fig. 2-4. Optical properties of NiO thin films. a) Ultraviolet-visible transmittance spectra of NiO films with different stabilizer conditions. Inset: enlarged transmittance spectra region between 320 ~ 470 nm. b) Tauc plots of different NiO thin films to determine optical bandgap .....46

Fig. 2-5. Atomic force microscopy images of bare ITO substrate in an area of  $5\ \mu\text{m} \times 5\ \mu\text{m}$ . RMS is the root mean square roughness of the film.....46

Fig. 2-6. Comparison of grazing incidence X-ray diffraction patterns of different NiO films with 20 nm thickness. a) full XRD patterns and magnified XRD patterns that belongs to b) (111) plane peak, c) (200) plane peak and d) (220) plane peak.....48

Fig. 2-7. Ultraviolet photoelectron spectroscopy (UPS) spectra of various NiO films. a) full UPS spectra and UPS spectra in the b) cutoff ( $E_{\text{cutoff}}$ ) energy regions and the c) onset ( $E_{\text{onset}}$ ) regions. d) Detailed energy diagram of different NiO and MAPbI<sub>3</sub> .....49

Fig. 2-8.  $J-V$  curves of hole only devices based on different NiO. The device structure is ITO / NiO / Au.....52

Fig. 2-9. X-ray photoelectron spectroscopy (XPS) spectra of NiO films with different stabilizers. Ni 2p<sub>3/2</sub> orbital of a) A-NiO, b) B-NiO, c) S-NiO, and O 1s orbital of d) A-NiO, e) B-NiO, f) S-NiO. The values in bracket resembles the area of deconvoluted peak.....53

Fig. 2-10. TOF-SIMS depth profiles measured in negative polarity of ITO/NiO/MAPbI <sub>3</sub> film. a) P-NiO, b) A-NiO, c) B-NiO, and d) S-NiO .....	54
Fig. 2-11. a) Optimized $J-V$ curves of PSC devices based on different HTM. $J-V$ curve of PSC under forward and reverse sweep direction with b) A-NiO c) B-NiO d) S-NiO .....	57
Fig. 2-12. a) Scanning transmission electron microcopy image of the fabricated PSC device. b) The corresponding element dispersive spectroscopy (EDS) mapping of the lateral structure of PSCs.....	58
Fig. 2-13. EQE spectra and integrated current density of perovskite solar cells based on different NiO .....	58
Fig. 2-14. The PCE distribution graph of PCE for 30 PSC devices based on a) A-NiO, b) B-NiO and c) S-NiO .....	59
Fig. 2-15. The distribution graph for different photovoltaic parameters a) $V_{oc}$ , b) $J_{sc}$ , and c) FF for 30 PSC devices based on different NiO .....	59
Fig. 2-16. Top-view scanning electron microscopy (SEM) images of MAPbI <sub>3</sub> perovskite films on top of a) A-NiO, b) B-NiO, and c) S-NiO at 50K magnification. d) Grain size distribution of perovskite films on different NiO. e) $J_{sc}$ and f) $V_{oc}$ values of PSCs with different NiO as function of light illumination intensity.....	60
Fig. 2-17. a) Top-view scanning electron microscopy (SEM) image of MAPbI <sub>3</sub> perovskite film on top of P-NiO. b) Grain size distribution of perovskite films on P-NiO.....	60
Fig. 2-18. Contact angle of MAPbI <sub>3</sub> solution droplet on different NiO films. a) P-NiO, b) A-NiO, c) B-NiO and d) S-NiO, and e) results plotted on a graph .....	63
Fig. 2-19. Dark $J-V$ characteristics of PSC devices based on different NiO. ....	63
Fig. 2-20. Images of different NiO solution with varying stabilizer conditions and its pH value measured by pH paper and pH meter.....	65

Fig. 2-21. Air stability of encapsulated devices based on different hole transporting materials. The inset shows the corresponding image of perovskite solar cell devices with glass encapsulation.....65

Fig. 3-1. Molecular structure and dipole moment of a) hydroquinone sulfonic acid potassium (HSA-K) salt and b) hydroquinone sulfonic acid sodium (HSA-Na) salt calculated by DFT calculation using Gaussian B3LYP 6-31G(d). X-ray photoelectron spectroscopy spectra of c) NiO and NiO:HSA-K for K 2p and S 2p orbital, d) NiO and NiO:HSA-Na for Na 1s and S 2p orbital. Ultraviolet photoelectron spectroscopy (UPS) spectra in the cutoff energy regions and their respective work function for NiO films with different amount of e) HSA-K salt and f) HSA-Na salt.....78

Fig. 3-2. a)  $J$ - $V$  curves of PM6:Y6-BO-4F OSC devices based on different NiO solutions. b)  $J$ - $V$  curves of PM6:Y6-BO-4F OSC devices without HTM (bare ITO) and with NiO as HTM.....79

Fig. 3-3. a) Ultraviolet-visible transmittance spectra of different NiO films from 250 to 900 nm. b) Tauc plots of different NiO thin films to determine optical bandgap. ....79

Fig. 3-4. a) AFM height images of ITO, ITO/NiO, ITO/NiO:HSA-K and ITO/NiO:HSA-Na. b) 3D AFM images .....81

Fig. 3-5. Grazing-angle X-ray diffraction (GI-XRD) patterns of different NiO films. a) Full XRD patterns and magnified XRD patterns that belongs to b) ●: (111) plane peak, c) ▲: (200) plane peak and d) ■: (220) plane peak .....82

Fig. 3-6. a) Full UPS spectra and b) UPS spectra in the cutoff ( $E_{cutoff}$ ) energy regions for NiO films. Schematic energy level diagram of c) vacuum level for NiO and vacuum level shift induced by the dipole formation at the surface of NiO using d) HSA-K, and e) HSA-Na.....84

Fig. 3-7. a) Device configuration and its energy diagram used in this study. b) Molecular structure of PM6 and Y6-BO-4F. Variation of work function and open-circuit voltage depending on the volume ratio of c) HSA-K and d) HSA-Na in NiO. e) $J$ - $V$ curves of optimized OSC devices with different NiO .....	86
Fig. 3-8. $J$ - $V$ curves of PM6:Y6-BO-4F OSC devices using a) NiO / HSA-K and b) NiO / HSA-Na. HSA based salts were tested from 1.0 ~ 10.0 mM concentration.	86
Fig. 3-9. $J$ - $V$ curves of PM6:Y6-BO-4F OSC devices based on NiO with different volume ratio of a) HSA-K and b) HSA-Na salt .....	88
Fig. 3-10. $J$ - $V$ curve of PM6:Y6-BO-4F OSC device based on PEDOT:PSS .....	90
Fig. 3-11. $J$ - $V$ curves of hole only devices based on different NiO. The device structure is as follow: ITO/NiO/Au.....	90
Fig. 3-12. Air stability of encapsulated OSC devices based on different HTMs ...	91
Fig. 3-13. a) Molecular structure of PCE-10 and PC <sub>71</sub> BM. b) $J$ - $V$ curves of optimized fullerene based OSC devices made of ITO/HTM/PCE-10:PC <sub>71</sub> BM/PFN-Br/Al with different HTMs.....	92

# Chapter 1. Introduction

## 1.1 Overview of photovoltaics

Energy is one of the most important issues in 21<sup>st</sup> century. As the effects of climate change and global warming become more pronounced, global attention and demand for environmental-friendly renewable energy are constantly growing. Since the start of industrialization in 2010s, the carbon dioxide (CO<sub>2</sub>) content in the atmosphere, which is one of the main causes of greenhouse effect, have risen sharply (**Figure 1-1**). Thus, at Paris Agreement on 2015, almost all countries have agreed to reduce greenhouse gas emissions and impede climate change by replacing fossil fuel based energy sources with five representative renewable energy sources such as solar, wind, hydro, geothermal and biomass (**Figure 1-2**). Among them, due to the abundant and sustainable solar energy, photovoltaics which convert sunlight into electricity became one of the most important energy production technology and research area. In order to commercialize these photovoltaic technologies and utilize them for practical application, photovoltaic cells must be highly efficient and stable.

The term photovoltaic is a combination of the Greek word phos, photos (light, of the light) and the name of the Italian physicist Alessandro Volta (1745-1825), who discovered the first functional electro-chemical battery and the unit of electricity, Volt. The basic component of photovoltaic is solar cell that consist of a semiconductor with p-n junction. When the solar cell is illuminated, charge carriers are generated and transported by the electrical field to the outer contacts. The result at the contacts of the solar cells is the creation of a voltage with released current. In order to achieve a usable voltage in the region of 20 – 50 V, many solar cells are

switched together in series to form a solar module.<sup>[1]</sup>

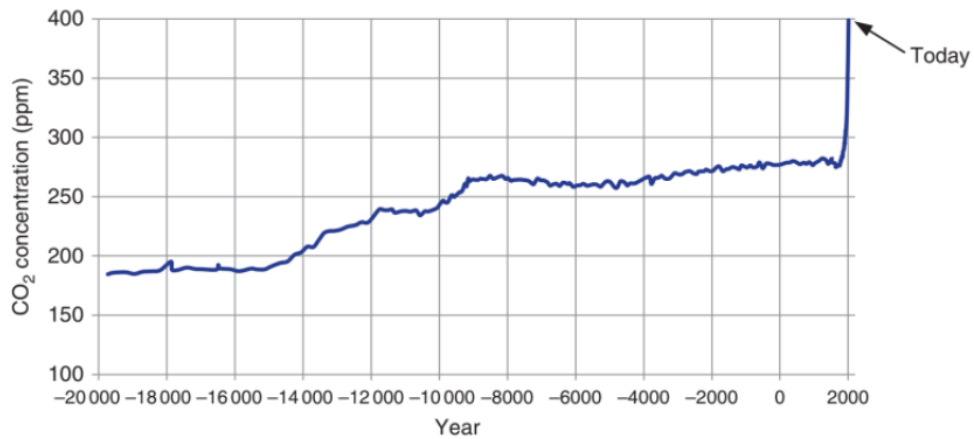


**Figure 1-1.** Development of CO<sub>2</sub> content in the atmosphere in the last 22,000 years. Noticeable is the steep rise since the start of industrialization. From Ref. [1]

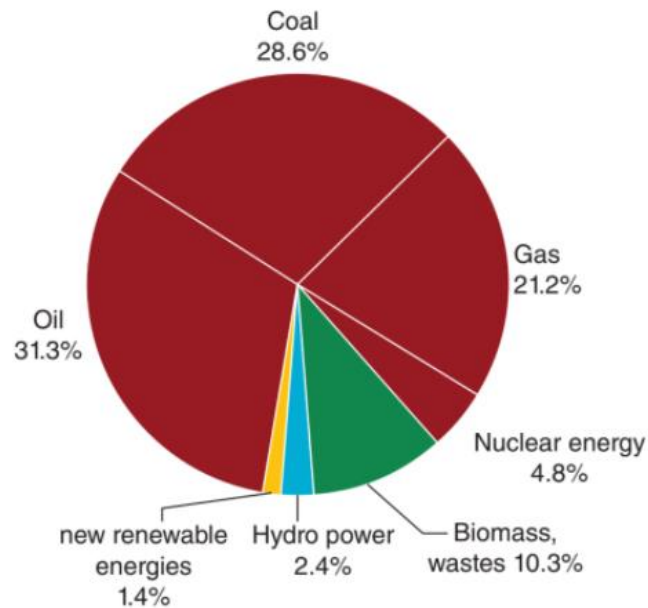


**Figure 1-2.** Distribution of worldwide energy consumption in 2014. From Ref. [1]

The first solar cell was developed in 1954 by Daryl Chapin, Calvin Fuller and

Gerald Pearson in the Bell Labs demonstrating silicon solar cell with an area of 2 cm<sup>2</sup> and 6% efficiency.<sup>[2]</sup> The photovoltaic effect were then accurately defined as the generation of voltage and electric current in a material (p-n junction) upon exposure to light.

Until now, majority of the commercialized photovoltaic cells are silicon based solar cells which demonstrate approximately 26% efficiency. However, since these silicon solar cells are highly energy demanding with significant thickness originating from its indirect bandgap and relatively weak absorbance, immense amount of research and development both from the industry and academy are being made for next-generation emerging photovoltaics. Unlike the conventional silicon based solar cells, these emerging solar cells can be flexible, transparent and lightweight which can provide broader possibility for diverse applications such as building integrated photovoltaics (BIPV) and solar assisted transportations (airplanes, boats and vehicles, etc.).

## 1.2 Emerging photovoltaics

The classification of photovoltaic technology has developed over three generations (**Figure 1-3**).<sup>[3]</sup> The first generation photovoltaic cells are wafer based crystalline silicon solar cells which still cover more than 90% of the market share. However, these solar cells are hundreds of micrometers-thick, require complicated fabrication processes and are very costly. The second generation photovoltaics are thin film based solar cells such as copper indium gallium selenide (CuInGaS<sub>4</sub>, CIGS), cadmium telluride (CdTe) solar cells. These materials are direct band gap semiconductors which can absorb light more efficiently than silicon, thus reducing



the thickness and cost of material. However, these solar cells demonstrated limited power conversion efficiency, and were also composed of toxic or rare-earth materials. The third generation photovoltaics are the emerging photovoltaic cells with relatively more softer materials such as quantum dot solar cells, dye sensitized solar cells (DSSCs), perovskite solar cells (PSCs) and organic solar cells (OSCs). Among them, PSCs and OSCs have gone through dramatic enhancement in certified power conversion efficiency over the past few years, demonstrating their potential as next-generation solar cells (**Figure 1-4**).

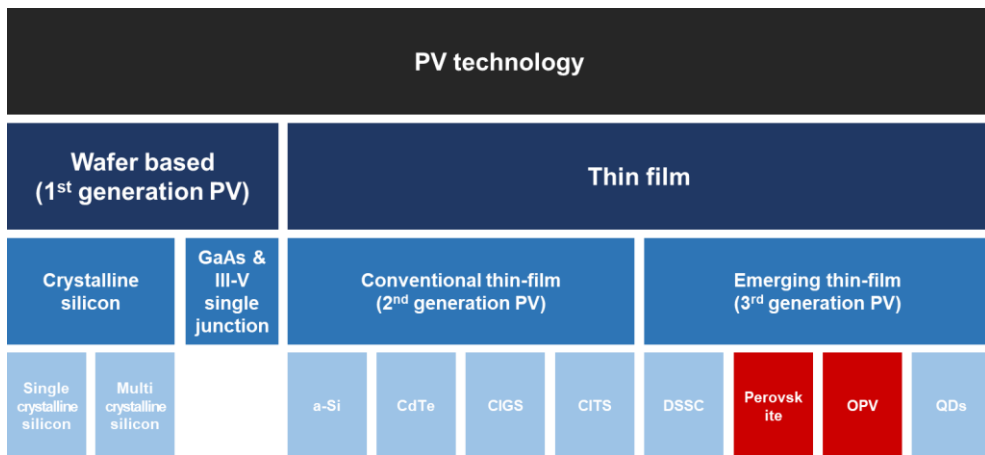


**Figure 1-3.** Different generation photovoltaics. From Ref [3].

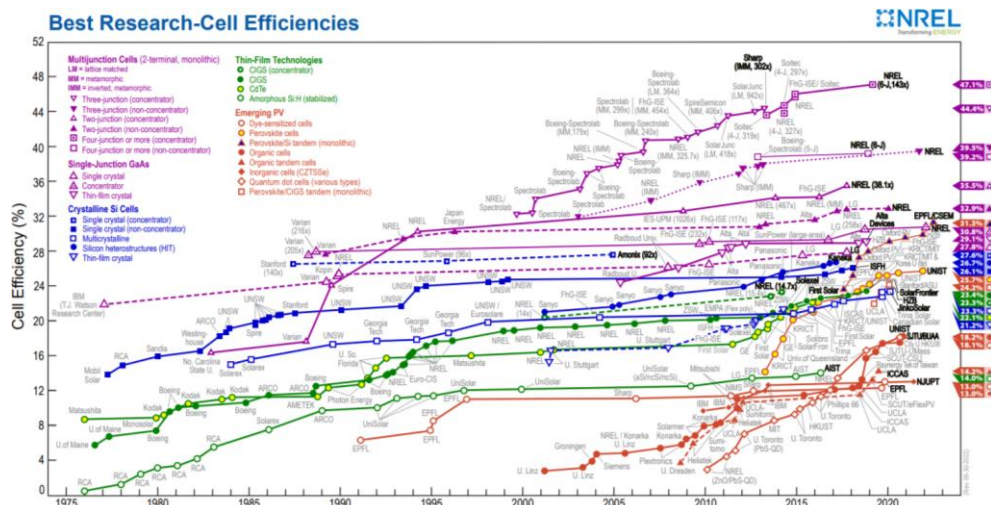


**Figure 1-4.** Best research-cell efficiency chart with highest confirmed conversion efficiencies for different types of cells from 1976. From NREL chart.

### 1.2.1 Perovskite solar cells

Perovskite is organic-inorganic hybrid material with  $ABX_3$  crystal structure where A is monovalent cation (Formamidinium (FA), Methylammonium (MA), Cs), B is divalent cation (Pb, Sn) and X is halide anion (I, Br, Cl).<sup>[4]</sup> These perovskite materials demonstrated numerous outstanding characteristics as light-absorbing material such as tunable direct bandgap ( $\sim 1.5$  eV), high absorption coefficient ( $10^{4-5}$  cm<sup>-1</sup>), small exciton (electron-hole pair) binding energy ( $\sim 10$  meV), long exciton diffusion length ( $\sim 1$   $\mu$ m) and low processing temperature ( $< 150^\circ\text{C}$ ).<sup>[5]</sup>

The first perovskite solar cells (PSCs) were reported by Prof. Miyasaka group with approximately 3% efficiency in 2009 based on methylammonium lead halide ( $\text{MAPbX}_3$  where  $X = \text{Br}$  and  $\text{I}$ ) and  $\text{TiO}_2$  and liquid electrolyte.<sup>[6]</sup> Due to the instability of perovskite materials in highly polar liquid electrolyte, after the replacement of liquid electrolyte with solid-state hole conductors such as spiro-OMeTAD (2,2',7,7'-Tetrakis[N,N-di(4-methoxyphenyl)amino]-9,9'-spirobifluorene), remarkable enhancement of PSCs were obtained achieving PCE near 10%. Afterwards, with intensive research and innovative strategies, certified PCE of PSCs have now reached up to 25.7%, which is comparable to that of silicon based solar cell. The rapid development of PSCs have been accompanied by modification on perovskite absorber materials, development of novel charge (hole and electron) transporting materials, and also interface engineering.

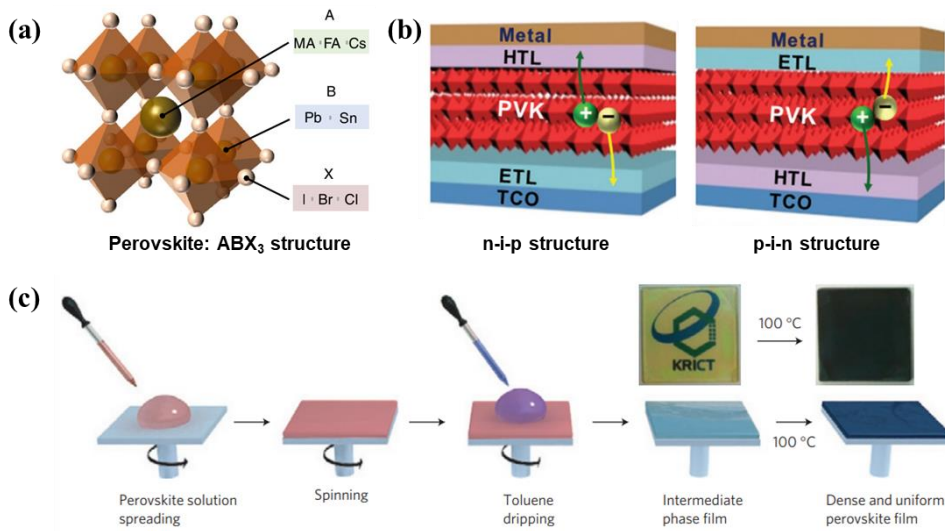


**Figure 1-5.** a)  $ABX_3$  perovskite crystal structure and b) n-i-p and p-i-n perovskite solar cell architecture and c) perovskite film fabrication process using solution process. From Ref. [4, 5]

## 1.2.2 Organic solar cells

Organic solar cells (OSCs) are composed of carbon-based organic semiconductor materials including donor and acceptor material as light absorbing materials. Compared to inorganic semiconductors or perovskite materials, organic semiconductors have a much lower dielectric constant (generally between 2 ~ 4) and thus, upon absorption of a photon with appropriate wavelength, excitons with high exciton binding energy are generated. Therefore, in order to separate these tightly bound excitons into separate charges (holes and electrons), sufficient driving force is needed for OSCs.

The working principle of OSCs can be divided into five different steps (**Figure 1-6**).<sup>[7]</sup> First is i) light absorption and exciton generation of the photoactive material, then is the ii) exciton diffusion to the donor-acceptor interface where iii) exciton

dissociation can then happen. Once the exciton is separated into electron and holes, iv) charge transport to the respective electrode and finally v) charge collection at the electrode takes place. The external quantum efficiency (EQE) which is the ratio of the number of electrons collected in the external circuit to the number of incident photons are expressed using the above five steps.

$$EQE = \eta_A \eta_{diff} \eta_{diss} \eta_{tr} \eta_{cc}$$

The first OSCs were reported by Prof. Tang group in 1986 demonstrating 1% efficiency using two (bi-layer) organic layers as the absorber (donor and acceptor) material.<sup>[8]</sup> Due to the short diffusion length of excitons (~ 10 nm) compared to the thickness of the active layer (~ 100 nm), the excitons recombined before reaching the donor-acceptor interface, thus limiting the efficiency of bi-layer solar cells. Therefore, a tradeoff existed between short exciton diffusion length and the minimum thickness of active layer to efficiently absorb the sunlight

This drawback was overcome by Heeger group in 1995 with bulkheterojunction (BHJ) concept by employing a bi-continuous network of donor and acceptor material with nanoscale phase separation.<sup>[9]</sup> This was especially successful in solving the tradeoff between thickness of active layer and short exciton diffusion length by creating numerous intimate donor and acceptor interfaces, thus allowing effective exciton dissociation and increasing charge collection.

Another recent innovation which contributed to the surge of OSCs PCE was the development of non-fullerene acceptor materials such as Y6.<sup>[10]</sup> Compared to the conventional rigid and bulky fullerene based acceptor materials, these small molecules are narrow band gap materials that have high absorbance complementary

with the absorbance of the donor (**Figure 1-7**).<sup>[11]</sup>

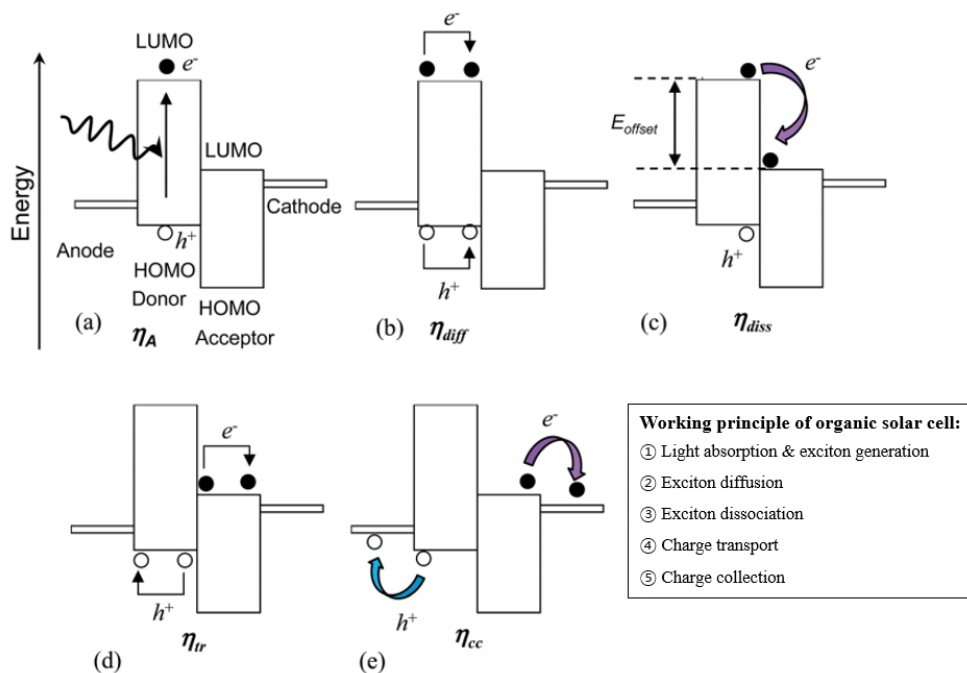


**Figure 1-6.** Working principle of organic solar cell and external quantum efficiency.

From Ref. [7]

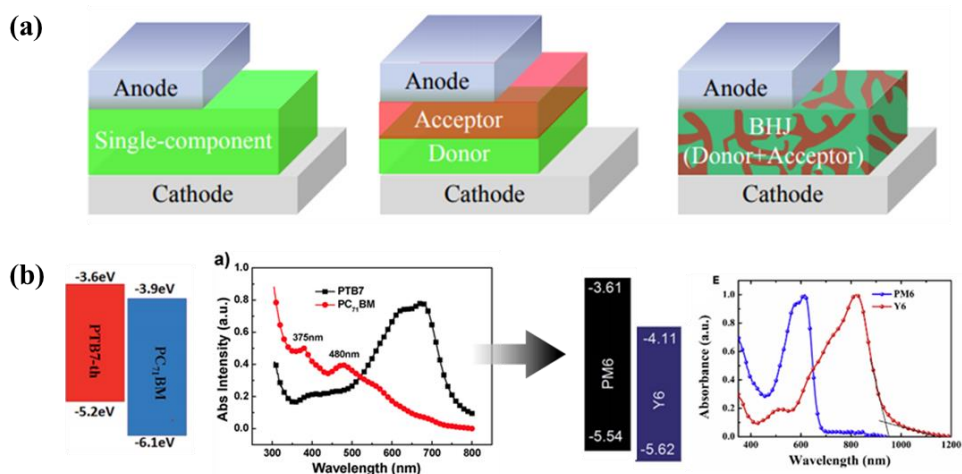


**Figure 1-7.** The development of organic solar cell with the invention of a) bulkheterojunction and b) non-fullerene acceptors. From Ref. [10, 11]

### 1.3 Device characterization

The basic characteristics of solar cell devices can be understood from its current-voltage ( $J$ - $V$ ) characteristics (**Figure 1-8**) which correspond the principle of a photodiode.<sup>[12]</sup> An illuminated solar cell provides a certain photocurrent at certain photovoltage. It is comprised of open-circuit voltage ( $V_{oc}$ ), short-circuit current ( $J_{sc}$ ), fill factor (FF) and power conversion efficiency (PCE).  $V_{oc}$  and  $J_{sc}$  are values of photovoltage and photocurrent when the power is zero ( $V_{oc}$  when  $J = 0$  and  $J_{sc}$  when  $V = 0$ ).<sup>[13]</sup> The maximum power generated by the solar cells (maximum power point, MPP) corresponds to the largest area rectangle within the  $J$ - $V$  curve

$$P_{MPP} = J_{MPP} \times V_{MPP}$$

where  $J_{MPP}$  and  $V_{MPP}$  are the corresponding current and voltage at the MPP. The FF is the ratio of the areas of rectangles defined by  $J_{sc}$  and  $V_{oc}$  to that of  $P_{MPP}$ .<sup>[14]</sup>

$$FF = \frac{J_{MPP}V_{MPP}}{J_{sc}V_{oc}}$$

The power conversion efficiency (PCE) is the ratio of maximum power generated by the cell to the power of sunlight ( $P_{sun}$ ).

$$PCE = \frac{P_{MPP}}{P_{sun}} = \frac{J_{MPP}V_{MPP}}{P_{sun}} = \frac{J_{sc}V_{oc}FF}{P_{sun}}$$

From the above equation, an efficient solar cell will have a high short-circuit current ( $J_{sc}$ ), a high open-circuit voltage ( $V_{oc}$ ) and a fill factor, FF, as close as possible to 1.

At open circuit ( $J = 0$ ), the  $V_{oc}$  of a solar cell can be obtained by

$$V_{oc} = \frac{k_B T}{q} \ln \left( \frac{J_{sc}}{J_o} + 1 \right)$$

which is logarithmically proportional to the short-circuit current and to the reciprocal of the reverse saturation current  $J_o$ .

Thus, the design and operation of an efficient solar cell should minimize the recombination rates throughout the device and also maximize the absorption of photons.<sup>[15]</sup>

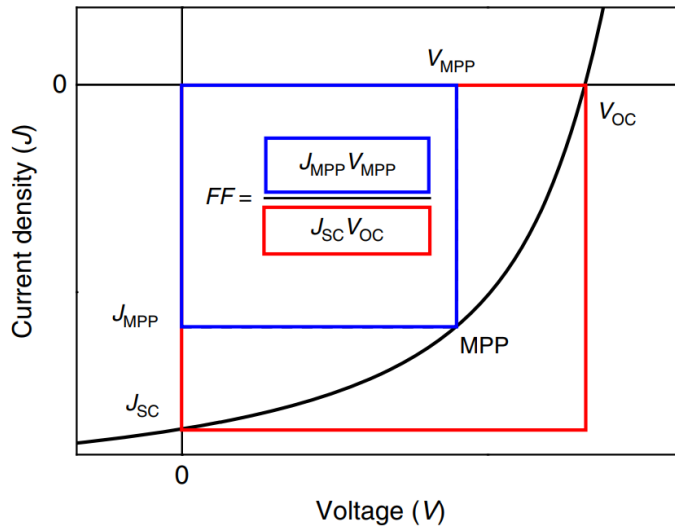


**Figure 1-8.**  $J$ - $V$  characteristic and parameters in solar cells. From Ref. [12]

### 1.3.1 Charge transport

Charges (electrons and holes) in a semiconductor behave like a free particle and thus they are subject to the classical process of drift and diffusion. Diffusion is the tendency of electrons and holes in a semiconductor to move from regions of high concentration to low concentration. In absence of external forces, the charges will tend to distribute themselves evenly. Drift is a charged particle's response to an applied electric field. When electric field is applied to a semiconductor, the energy



bands bend upward in the direction of the applied electric field. While the negatively charged electrons in the conduction band move in the opposite direction to the applied field, positively charged holes in the valence band move in the same direction to the applied field. In other words, electrons sink and holes float. In real devices, charge transport in general is induced by the intrinsic electric field generated by the difference in the work functions of the two asymmetric electrodes. However, there are numerous additional features and obstacles to consider and overcome in order for the charges to be collected effectively at the electrodes.<sup>[15]</sup>

One of the main obstacles is the contact between the active layer and adjacent layers. The energetic difference, imperfect adhesion, and charge accumulation at the interface can create barriers for charge extraction and diminish  $V_{oc}$  and FF. Insertion of suitable charge transporting materials with well-aligned energy level and great contact can effectively alleviate these barriers. Therefore, selection and application of appropriate charge transporting materials have become extremely important.

### **1.3.2 Charge recombination**

Charge recombination is also another important phenomenon that we must know in photovoltaics. When solar cell absorbs photons (incident light), electron-hole pairs (excitons) are generated. However, even after these excitons are dissociated into holes and electrons, due to the coulombic attraction or charge traps and accumulation, these holes and electrons can recombine again into excitons. These unwanted recombination of holes and electrons degrade overall device efficiency.

There are two different types of recombination, geminate recombination and non-geminate recombination (**Figure 1-9**). Geminate recombination is the process where

charges originating from the same exciton recombine. Geminate recombination is of particular concern for the OSCs due to the small dielectric constant of organic materials which leads to higher possibility of coulombic interaction between geminate charges. Non-geminate recombination, also referred to as bimolecular recombination, is the process where charges from different sources (different excitons or from the contacts) meet and recombine. Non-geminate recombination is triggered mainly due to the limited mobility of the charges or traps and defects.<sup>[16]</sup>

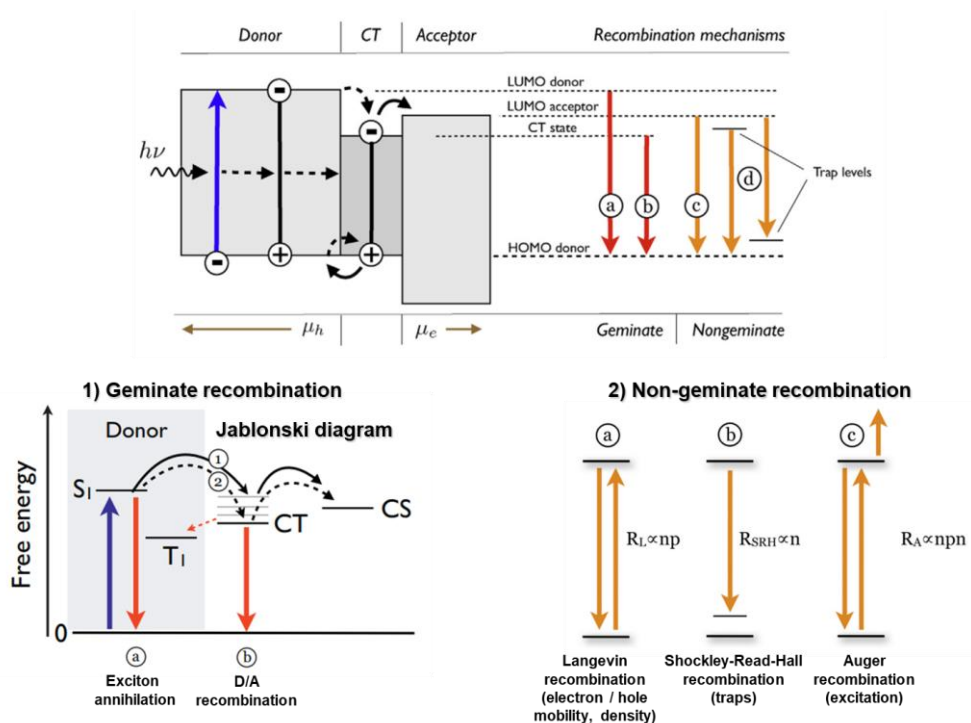


**Figure 1-9.** Charge transport and recombination mechanisms in solar cells. From Ref. [16]

## 1.4 Charge transporting materials

The most important aspect of high performance photovoltaics is undoubtedly the active layer, where charge carriers are generated and dissociated into holes and electrons. However, in typical solar cells, in order for these holes and electrons to be collected at the anode and cathode, additional layers are interposed between the active layer and these electrodes. These layers are referred to charge transporting layers (or either interfacial layers or buffer layers) and are essential to fabricate high performance solar cells (**Figure 1-10**). Therefore, suitable selection of materials and understanding of the roles and influence of charge transporting materials must be carefully considered.<sup>[17]</sup>

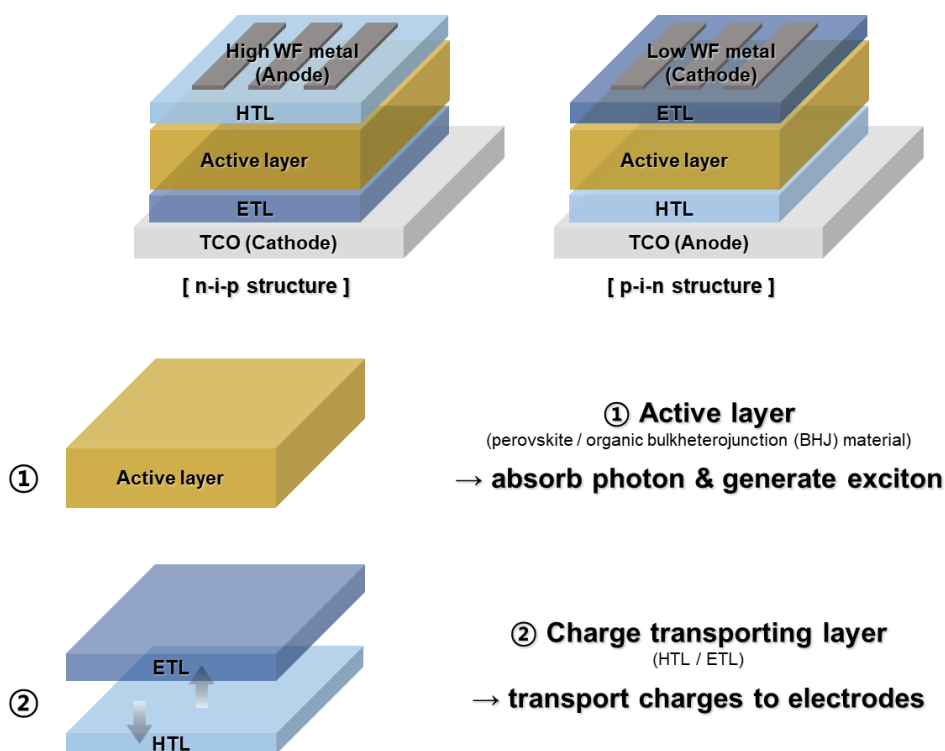


**Figure 1-10.** Structure of solar cell which is composed of active layer and charge transporting layers.

### 1.4.1 Hole transporting materials

Both PSCs and OSCs can be divided into two different architectures, n-i-p (conventional structure for PSC and inverted structure for OSC) and p-i-n (inverted structure for PSC and conventional structure for OSC) structure. Compared to n-i-p structure, the p-i-n structure have the advantages of low-temperature solution, lower price, flexible device.

Hole transporting materials (HTMs) in p-i-n structure should have appropriate energy level to not only transport holes effectively from the active layer to the anode but also block electrons from leaking to the anode, which can greatly reduce recombination of electrons and holes at the interface between perovskite and HTM. Furthermore, since these HTMs lie underneath the perovskite layer, they should have high transmittance in order to prevent any parasitic absorption of sunlight before reaching the perovskite layer. In addition, HTMs should also have solvent orthogonality to the solvents used in the active layer, and have smooth and uniform morphology since they can influence the morphology of the perovskite layer fabricated on top.<sup>[18]</sup>

Until now, the most commonly used hole transporting material (HTM) for both PSC and OSC is poly(3,4-ethylenedioxythiophene) polystyrene sulfonate (PEDOT:PSS). PEDOT:PSS is a commercialized organic polymer material with high transparency, high conductivity, and good film-forming property that is now applied in numerous organic electronic applications.

Nevertheless, PEDOT:PSS have significant drawbacks. Due to the acidity of PSS chain and its dispersion in water, PEDOT:PSS is intrinsically acidic and hygroscopic,

which triggers device degradation. Alternatively, p-type inorganic oxides have gained great amount of attention due to their advantages of low cost, ease of synthesis and high stability.

### **1.4.2 Metal oxide**

Metal oxides are chemical compounds that contain at least one oxygen atom and one other element in its chemical formula. Almost the entire Earth's crust is made of oxides as the elements of crust are oxidized by the oxygen present in the atmosphere or in the water. Therefore, in general, metal oxides can be considered as naturally abundant and stable compounds. Metal oxides cover broad spectrum of electronic properties from insulators to semiconductors, metallic conductors and superconductors. The wide variety of materials with different electronic, optical and chemical characteristics, and also with their ability superior thermal and chemical stability make metal oxides a potential candidate to apply in photovoltaics.<sup>[19]</sup>

Semiconductor metal oxides have been utilized in photovoltaic devices for decades and have made significant contribution in the progress and development of photovoltaics. Several metal (mainly transition metals) oxides have been reported as efficient charge transporting materials for photovoltaics. High work function oxides such as  $\text{MoO}_3$ ,  $\text{WO}_3$ ,  $\text{V}_2\text{O}_5$ ,  $\text{NiO}$ ,  $\text{Cu}_2\text{O}$  have been used at the anode and low work function oxides such as  $\text{TiO}_2$ ,  $\text{ZnO}$ ,  $\text{SnO}_2$  have been used at the cathode.<sup>[20]</sup> The thickness of these metal oxide layers is typically in between 5 to 30 nm. Depending on the material and deposition technique, metal oxides demonstrate different morphologies from compact layers to nanoparticles and nanorods.

The fabrication method of metal oxide is very simple, low-cost and easily scalable.

Among various metal oxide fabrication methods, solution processed metal oxide thin film is one of the most successful and commonly used preparation methods due to the compatibility with commercialized roll to roll fabrication and demands for large area device fabrication.<sup>[18]</sup>

Sol-gel chemistry of metal oxide can be divided into aqueous sol-gel process which involves water and non-aqueous sol-gel process which involves organic solvents. The former is more complicated and disadvantageous due to the high reactivity of metal oxide precursor towards water and also since there are several reaction parameters that have to be strictly controlled such as hydrolysis and condensation, pH, temperature, and rate of oxidation, etc.

On the other hand, non-aqueous sol-gel process using surfactant involves transformation of the precursor species into oxidic compound in the presence of stabilizing ligands (stabilizers) in a typical temperature range of 250 to 350 °C.<sup>[21]</sup> These stabilizers provide outstanding control over the growth of metal oxide, leading to uniformly dispersed samples. Furthermore, the ability of surfactants to cap the surface of the nanoparticles allows advantages such as shape control, low agglomeration tendency, high dispersibility in organic solvents, and the potential to modify surface properties.<sup>[22]</sup>

### **1.4.3 Nickel oxide**

The first and prevalent p-type metal oxide is nickel oxide (NiO) with cubic rock-salt (NaCl) structure since 1993.<sup>[23]</sup> NiO have wide optical bandgap (3.6 ~ 4.0 eV) and high stability with also low material cost. The work function and energy level of NiO can be easily modified between 4.5 ~ 5.6 eV by control of deposition conditions

and surface treatments.<sup>[24]</sup> The tunable energy level of NiO is advantageous to feasibly match the energy levels of diverse active layers including perovskite and organic BHJ materials.

The electron occupation of NiO is  $\text{Ni}3d^8 \text{O}2p^6$ . Pure stoichiometric NiO (Ni:O = 1:1) are insulators with electrical conductivity lower than  $10^{-11} \text{ S cm}^{-1}$ . The semiconducting NiO and p-type NiO that are used in optoelectronic devices is non-stoichiometric, with metal-deficient (Ni < O) NiO (**Figure 1-11**).<sup>[25]</sup> The metal deficient or oxygen excess characteristic results in Ni vacancies ( $\text{Ni}^{3+}$ ) which act as free holes and makes NiO a p-type semiconductor. The hole conductivity of NiO is determined by these Ni vacancies and can also be adjusted by controlling the ratio or amount of  $\text{Ni}^{3+}$ .<sup>[26]</sup>

Fabrication methods of NiO include sputtering, electron beam evaporation, spray pyrolysis, pulsed laser deposition, atomic layer deposition, combustion and sol-gel technique. These excellent characteristics of NiO make it a potential candidate as HTM for photovoltaics.

The first application of NiO in OSC was carried out by Tobin J. Marks group in 2008 using pulsed-laser deposition method to fabricate NiO as anode interfacial layer for polymer BHJ OSCs.<sup>[27]</sup> With P3HT and PCBM as donor and acceptor material, it demonstrated 5% efficiency. The first application of NiO in PSC was reported by Henry Snaith group in 2013 using spin-coated NiO.<sup>[28]</sup> However due to the poor perovskite film coverage on top of NiO, the efficiency was limited to less than 1%. Since then, significant amount of studies and researches were devoted to develop NiO as effective HTM for photovoltaic devices. NiO is now definitely one of the

most promising HTM candidates for both PSCs and OSCs.

**NiO : “metal-deficient” semiconductor** (metal < oxygen)  $\text{Ni}_1\text{O}_1 \rightarrow \text{Ni}_2\text{O}_3$

→ conduction dominated by **vacancies / impurities** ( $\text{Ni}^{3+}$  / lattice defects)

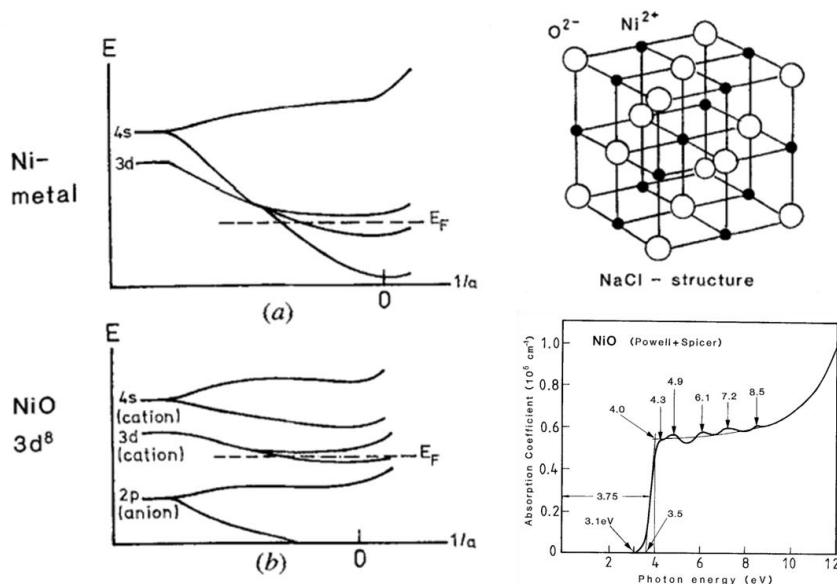


**Figure 1-11.** Band structure of Ni metal and NiO. Cubic rocksalt (NaCl) structure of NiO and absorption coefficient of NiO. From Ref. [25]

## 1.5 Research objectives and outlines

This dissertation is focused on developing nickel oxide (NiO) as effective hole transporting materials for high performance photovoltaics such as perovskite solar cells (PSCs) and organic solar cells (OSCs). Studies on diverse modification approaches of NiO that resulted from novel material properties, synergistic and innovative solar cell concepts, leading to in-depth understanding of photovoltaics are provided. The following contents consist of two chapters (**Figure 1-12**):

In chapter 2, we utilize pH-controlled NiO based on virtually neutral ammonium salt stabilizers to improve both efficiency and stability of PSCs. With the comparison



of two other conventional stabilizers used in sol-gel NiO; hydrochloric acid (HCl) and monoethanolamine (MEA), we found NiO films with different stabilizers demonstrated different morphological and optoelectronic properties. Furthermore, NiO with ammonium salt stabilizer enhanced interfacial properties between NiO and perovskite layer and improved quality of perovskite layer atop. With optimum NiO containing ammonium salt, our champion PSC exhibited PCE of 19.91% with notably high  $V_{oc}$  of 1.13 V based on methylammonium lead iodide (MAPbI<sub>3</sub>) PSCs. In addition, NiO with salt stabilizer demonstrated outstanding device stability maintaining over 97% of its initial PCE even after 800 hours in ambient condition.

In chapter 3, we utilize hydroquinone sulfonic acid (HSA) salts which possess dipole moment to overcome the energetic barrier between inorganic NiO HTM and organic bulkheterojunction (BHJ) layer. HSA potassium and sodium salts with ionic groups induce work function modulation and hole transport enhancement of NiO layer. With PM6 and Y6-BO-4F as BHJ material, using NiO with addition of HSA based salts, we were able to obtain significant improvement in  $V_{oc}$  from 0.79 V to 0.86 V and achieve high PCE of 14.19% which is comparable to that of PEDOT:PSS. Furthermore, for 1200 hours under ambient atmosphere, OSCs based on NiO containing HSA salts demonstrated enhanced stability compared to that of PEDOT:PSS.

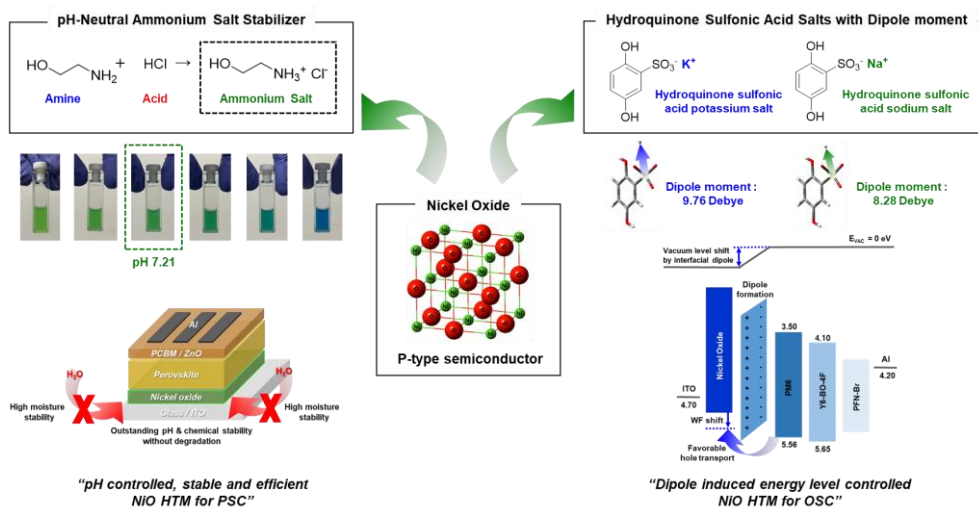


**Figure 1-12.** An overview of each chapter of this dissertation

## 1.6 Bibliography

- [1] K. Mertens, *Somerset, GB: Wiley*.
- [2] D. M. Chapin, C. S. Fuller, G. L. Pearson, *Journal of applied physics* **1954**, *25*, 676.
- [3] R. Peleg, *The Perovskite Handbook (2018 Edition)*, Lulu.com, **2018**.
- [4] Y. Zhou, L. M. Herz, A. K. Y. Jen, M. Saliba, *Nat. Energy* **2022**, *7*, 794.
- [5] a) N. J. Jeon, J. H. Noh, Y. C. Kim, W. S. Yang, S. Ryu, S. I. Seok, *Nature Materials* **2014**, *13*, 897; b) A. Rajagopal, K. Yao, A. K.-Y. Jen, *Adv. Mater.* **2018**, *30*, 1800455.
- [6] A. Kojima, K. Teshima, Y. Shirai, T. Miyasaka, *J. Am. Chem. Soc.* **2009**, *131*, 6050.
- [7] J. Yan, B. R. Saunders, *RSC Advances* **2014**, *4*, 43286.
- [8] C. W. Tang, *Appl. Phys. Lett.* **1986**, *48*, 183.
- [9] G. Yu, J. Gao, J. C. Hummelen, F. Wudl, A. J. Heeger, *Science* **1995**, *270*, 1789.
- [10] a) J. Yuan, Y. Zhang, L. Zhou, G. Zhang, H.-L. Yip, T.-K. Lau, X. Lu, C. Zhu, H. Peng, P. A. Johnson, M. Leclerc, Y. Cao, J. Ulanski, Y. Li, Y. Zou, *Joule* **2019**, *3*, 1140; b) M.-A. Pan, T.-K. Lau, Y. Tang, Y.-C. Wu, T. Liu, K. Li, M.-C. Chen, X. Lu, W. Ma, C. Zhan, *J. Mater. Chem. A* **2019**, *7*, 20713.
- [11] a) B. Tang, J. Liu, X. Cao, Q. Zhao, X. Yu, S. Zheng, Y. Han, *RSC Advances* **2017**, *7*, 17913; b) D. Huang, Y. Li, Z. Xu, S. Zhao, L. Zhao, J. Zhao, *Physical Chemistry Chemical Physics* **2015**, *17*, 8053.
- [12] T. Dittrich, *Materials concepts for solar cells*, World Scientific, **2015**.
- [13] S. R. Forrest, *Organic electronics: foundations to applications*, Oxford University Press, USA, **2020**.

- [14] D. Bartesaghi, I. d. C. Pérez, J. Kniepert, S. Roland, M. Turbiez, D. Neher, L. J. A. Koster, *Nature Commun.* **2015**, 6, 7083.
- [15] A. Luque, S. Hegedus, *Handbook of photovoltaic science and engineering*, John Wiley & Sons, **2011**.
- [16] C. M. Proctor, M. Kuik, T.-Q. Nguyen, *Progress in Polymer Science* **2013**, 38, 1941.
- [17] B. P. Rand, H. Richter, *Organic Solar Cells: fundamentals, devices, and upscaling*, CRC Press, **2014**.
- [18] G. Korotcenkov, *The Future of Semiconductor Oxides in Next-Generation Solar Cells*, Elsevier, **2017**.
- [19] G. Korotcenkov, *Solution processed metal oxide thin films for electronic applications*, Elsevier, **2020**.
- [20] S. S. Shin, S. J. Lee, S. I. Seok, *Adv. Funct. Mater.* **2019**, 29, 1900455.
- [21] J. Park, J. Joo, S. G. Kwon, Y. Jang, T. Hyeon, *Angewandte Chemie International Edition* **2007**, 46, 4630.
- [22] M. Niederberger, N. Pinna, *Metal oxide nanoparticles in organic solvents: synthesis, formation, assembly and application*, Springer Science & Business Media, **2009**.
- [23] H. Sato, T. Minami, S. Takata, T. Yamada, *Thin Solid Films* **1993**, 236, 27.
- [24] S. Chen, J. R. Manders, S.-W. Tsang, F. So, *J. Mater. Chem.* **2012**, 22, 24202.
- [25] S. Hüfner, *Advances in Physics* **1994**, 43, 183.
- [26] X. Yin, Y. Guo, H. Xie, W. Que, L. B. Kong, *Sol. RRL* **2019**, 3, 1900001.
- [27] M. D. Irwin, D. B. Buchholz, A. W. Hains, R. P. H. Chang, T. J. Marks, *Proc. Natl. Acad. Sci. U.S.A.* **2008**, 105, 2783.

- [28] P. Docampo, J. M. Ball, M. Darwich, G. E. Eperon, H. J. Snaith, *Nature Commun.* **2013**, *4*, 2761.

## **Chapter 2. Nickel oxide hole transporting material employing ammonium salt stabilizer for high performance perovskite solar cells**

### **2.1 Research background**

Perovskite solar cells (PSCs) have gained great attention in the photovoltaic research field due to its potential as the next generation solar cell. From the first report of perovskite solar cell (PSCs) by Miyasaka's group in 2009 with 3.9% power conversion efficiency (PCE), certified PCE of 25.7% was achieved recently which is comparable to that of silicon based solar cells.<sup>[1]</sup> This meteoric rise could be realized by perovskite's outstanding optoelectronic properties such as low exciton binding energy, long exciton diffusion length, and facile bandgap tunability.<sup>[2]</sup> However, issues regarding long-term stability of PSC still remain as a challenge for commercialization.

Numerous researchers are making an ongoing effort to develop novel charge transporting materials since the overall performance of PSCs is often restrained by adjacent layers and interfacial properties rather than just the perovskite layer itself. In PSCs, various p-type materials have been applied as hole transporting materials (HTMs). The most widely used HTMs are organic HTMs such as 2,2',7,7'-tetrakis[N,N-di(4-methoxyphenyl)amino]-9,9'-spirobifluorene (Spiro-OMeTAD), poly(triaryl amine) (PTAA), and poly(3,4-ethylenedioxythiophene) polystyrene sulfonate (PEDOT:PSS). However, these organic HTMs are expensive and limited by their stability and scalability issues.<sup>[3]</sup> In particular, for inverted perovskite solar

cells, acidic pH of PEDOT:PSS corrodes neighboring layers and deteriorates device stability.<sup>[4]</sup> As a result, vast amount of studies have been conducted on the counterpart inorganic oxide HTMs. In particular, nickel oxide (NiO) is considered as one of the most promising HTMs for p-i-n inverted PSCs owing to its high stability, high mobility and low cost.<sup>[5]</sup>

There are several methods for NiO film fabrication from high vacuum deposition to solution processable methods.<sup>[6]</sup> Methods which require high vacuum and high cost procedures are not compatible with the commercial roll-to-roll process. Among the solution processes including NiO nanoparticle (NP) method which demands complicated NP fabrication procedures, sol-gel method is highly advantageous due to its simple and facile processing nature.<sup>[7]</sup>

To date, ongoing efforts have been made to modify NiO and improve performance of PSC. Various metal dopants such as Cu, Li, Cs, etc., have been doped into NiO to enhance intrinsic conductivity of NiO and thereby achieve higher short-circuit current ( $J_{sc}$ ).<sup>[8]</sup> Furthermore, organic molecules and self-assembled monolayers have also been used to modulate NiO's surface properties and enhance PCE.<sup>[9]</sup> However, until now, studies on NiO have focused more on improving conductivity and  $J_{sc}$  of NiO than on tuning open-circuit voltage ( $V_{oc}$ ) of NiO based PSC. As a result, although promising results have been obtained using NiO as HTM, majority of PSCs with NiO still exhibit lower  $V_{oc}$  ( $< 1.10$  V) compared to organic HTMs.<sup>[10]</sup> Moreover, these unstable dopants and heteroatoms trigger instability, parasitic absorption losses and solubility issues.<sup>[11]</sup> Therefore, a generically different method which can improve both  $V_{oc}$  and performance of sol-gel based NiO is needed.

While many reports have demonstrated diverse modification and processing

techniques to improve performance of PSCs with sol-gel NiO, they resulted in limited consensus on the usage and influences of stabilizers on NiO and performance of PSCs. According to numerous previous studies on NiO, during fabrication of sol-gel NiO, either acidic or alkaline stabilizer such as hydrochloric acid (HCl) and monoethanolamine (MEA) has always been added indispensably. Generally, these stabilizing agents are used as chelating agents and catalysts to prevent gelation of NiO and create homogeneous solution.<sup>[12]</sup> However, despite these necessities, the use of highly acidic and alkaline stabilizers should result in NiO solutions with biased pH and presumably degenerate the chemical stability of PSC.<sup>[13]</sup> Therefore, it is imperative to investigate the influence of these stabilizers and develop more stable stabilizer for NiO which can secure long-term device stability and boost its performance.

Here, we report a very novel strategy of using pH-controlled NiO based on virtually neutral ammonium salt to improve both efficiency and stability of PSCs. We have compared our ammonium salt based NiO with two conventional sol-gel NiO references; NiO with HCl and NiO with MEA. We have studied the influence of stabilizers on NiO's intrinsic property and device performance. NiO films with different stabilizers demonstrated different morphological and optoelectronic properties. Furthermore, NiO with ammonium salt stabilizer enhanced interfacial properties between NiO and perovskite layer and improved quality of perovskite layer atop. With optimum NiO containing ammonium salt, our best-performing PSC exhibited highest PCE of 19.91% with notably high  $V_{oc}$  of 1.13V based on methylammonium lead iodide (MAPbI<sub>3</sub>) PSCs and outstanding stability maintaining over 97% of its initial PCE even after 800 hours (h) in ambient condition with



encapsulation.

## **2.2 Experimental methods**

### **2.2.1 Material preparation**

Nickel acetate tetrahydrate (99.999 %) were purchased from Alfa Aesar and 2ME, HCl, MEA, lead iodide ( $\text{PbI}_2$ ) were purchased from Sigma Aldrich. PCBM were purchased from 1-material.

NiO solution was fabricated by dissolving nickel acetate tetrahydrate (0.3 m) in 2-methoxyethanol. For A-NiO, HCl (0.3 mol) was added, while for B-NiO, MEA (0.3 mol) was added. For S-NiO, HCl (0.3 mol) and MEA (0.3 mol) was added in NiO. The solution was stirred at 60 °C for 4 hours.

### **2.2.2 Perovskite solar cell fabrication**

Patterned ITO glass substrates were cleaned in deionized water, acetone and isopropanol (IPA) respectively, for 15 min, via ultrasonication before use. UV-Ozone was used to treat the substrates for 30 min. PEDOT:PSS (Clevios P VP AI 4083) solution was spin-coated on these cleaned substrates at the speed of 5000 rpm for 30 s, followed by annealing at 150 °C for 10 min. For NiO, solution was spin-coated at the speed of 4000 rpm for 30 s, followed by annealing at 300 °C for 30 min. The  $\text{MAPbI}_3$  solution was obtained by dissolving MAI (1 mol) and  $\text{PbI}_2$  (1 mol) in dimethylformamide (DMF) (635  $\mu\text{l}$ ) and dimethyl sulfoxide (DMSO) (71  $\mu\text{l}$ ).  $\text{MAPbI}_3$  precursor solution was spin-coated onto different HTM at the speed of 4000 rpm for 25 s. After 10 s had passed, diethyl ether (100  $\mu\text{l}$ ) was dropped onto the rotating film. The as-spun film was then annealed at 65 °C for 1 min and 100 °C for 2 min consecutively. Next, PCBM (30  $\text{mg ml}^{-1}$  in chlorobenzene) filtered by JP filter

was spin-coated onto the MAPbI<sub>3</sub> layer at the speed of 2000 rpm for 30 s. Afterward, ZnO np solution dispersed in 1-butanol was spin-coated onto the PCBM at the speed of 4000 rpm for 40 s. Finally, a 100-nm thick aluminum counter electrode was deposited by thermal evaporation under a vacuum of 10<sup>-6</sup> Torr.

### **2.2.2 Characterization.**

The pH values of the PEDOT:PSS and NiO solutions were measured with pH paper and pH meter (HANNA instruments). UV-vis spectra were recorded using (Shimadzu UV 2550) in the wavelength range 300nm to 850 nm. The energy level of different NiO films were obtained from UPS using AXIS-NOVA and Ultra DLD with Helium I (21.2 eV) as photon source. XPS spectra were measured using Electron Spectroscopy for Chemical Analysis (ESCA). Binding energies were referenced to the C-C bond of the C 1s region at 284.5 eV. XRD patterns were characterized by an X-ray diffractometer (Bruker D8-Advance). Surface SEM images were obtained FE-SEM (Tescan Mira 3 LMU FEG). AFM images were measured using NX-10 (Park Systems) and analysis area was 5  $\mu\text{m} \times 5 \mu\text{m}$ . STEM images were obtained by using JEM-2100F (JEOL Ltd.). TOF-SIMS were obtained from TOF-SIMS 5 (ION-TOF, Germany) under negative polarity with Cs<sup>+</sup> (1 keV, 100 nA, 500  $\times$  500  $\mu\text{m}^2$ ) as the etching source and Bi<sup>+</sup> (30 keV, 1 pA, 100  $\times$  100  $\mu\text{m}^2$ ) as the analyzing source. The current density-voltage ( $J$ - $V$ ) characteristics of the solar cells were measured using a Keithley 4200 source measurement unit. The solar cell performances were characterized under AM 1.5G condition with an illumination intensity of 100 mW cm<sup>-2</sup>, as generated using an Oriel Sol3A solar simulator (Oriel model 94023A). The  $J$ - $V$  curves of all the devices were measured by masking the active area using a shadow mask with an area of 0.05 cm<sup>2</sup> under ambient atmosphere.

Encapsulation of devices was done by simple glass (15 mm × 10 mm) encapsulation using UV resin XNR 5570 as the adhesive layer with 10 minutes of UV 365nm illumination to dry the resin.

## 2.3 Results and Discussions

Schematic preparation procedure of NiO is shown in **Figure 2-1a**. As can be seen, depending on the type and concentration of stabilizers, NiO solutions appear in different colors. The difference in color is due to the unfilled 3d shell of nickel and different metal-chelating agent binding.<sup>[12b]</sup> We prepared three kinds of NiO solution with different stabilizing agents. NiO solutions using different stabilizers are abbreviated as follows; P-NiO for pristine NiO without stabilizers, A-NiO for acidic HCl, B-NiO for basic MEA and S-NiO for salt. The details are described in Experimental Section.

We prepared S-NiO solution by two different methods. First, we synthesized ammonium salt formed by reacting HCl with MEA. In this case, an acid-base reaction mechanism as shown in **Figure 2-2** will occur, where the stabilizer product is in the form of ammonium salt. It is well established that reacting an amine ( $\text{RNH}_2$ ) with a solution of a strong acid (HCl) produces an ammonium salt ( $\text{RNH}_3^+\text{Cl}^-$ ).<sup>[14]</sup> The ammonium salt was added to NiO solution and the NiO solution was stirred for 24 h. Alternatively, we could exploit in-situ generation of ammonium salt by adding equimolar amount of HCl and MEA to NiO solution followed by stirring for 24 h. Since S-NiO prepared by both methods demonstrated identical photovoltaic performances, we conveniently prepared S-NiO solution by the latter in-situ method if not mentioned otherwise.

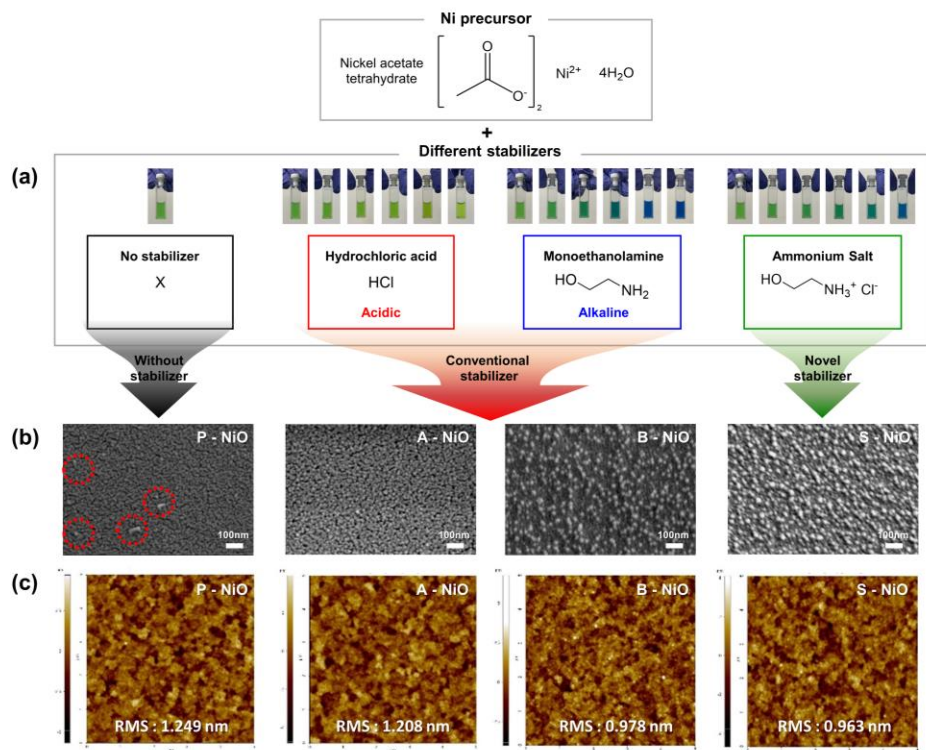


**Figure 2-1.** a) Schematic preparation procedure of NiO solution with different stabilizers and diverse concentration resulting in different NiO solution color. b) Top-view scanning electron microscopy images of NiO films with different stabilizer conditions at 100 K magnification. c) Atomic force microscopy images of NiO films with different stabilizer conditions in an area of  $5\ \mu\text{m} \times 5\ \mu\text{m}$ . RMS is the root mean square roughness of the film.

First, we fabricated PSC devices based on pristine NiO (P-NiO) in order to examine the necessity of stabilizers in NiO solution. As a result, PSC devices based on P-NiO demonstrated inferior performance compared to those based on NiO with stabilizers, approving the necessity of stabilizers in NiO (*vide infra*).

Images of NiO solutions with different stabilizers are shown in **Figure 2-3**. While P-NiO showed turbid greenish solution, all NiO solutions with stabilizers showed clear, and transparent greenish solution distinguished by difference in color. The transparent solution for S-NiO suggests that our strategy is effective in dissolving nickel precursor.

We prepared NiO films and measured ultraviolet-visible (UV-Vis) transmittance spectra of different NiO films as shown in **Figure 2-4a**. The inset image illustrates slightly improved transmittance for S-NiO thin film in the region of 350 ~ 600 nm compared to other types of NiO which is effective for perovskite layer to absorb more photon energy.

We carried out scanning electron microscopy (SEM) and atomic force microscopy (AFM) measurement to study morphology of different NiO films as shown in **Figure 2-1b and c**. As expected, due to the poor solubility of NiO without stabilizers, undissolved nickel precursors with size of tens of nanometers was observed in P-NiO film. This rough film morphology of P-NiO induces inevitable contact resistance and the undissolved particles can act as unfavorable charge recombination sites. In contrast, all NiO films with stabilizer did not exhibit any undissolved nickel precursors and showed different morphologies. The morphology of S-NiO film was relatively more uniform and compact than those of A-NiO and B-NiO films. This result is in agreement with the AFM results where S-NiO demonstrated the smallest

root mean square (RMS) roughness of 0.963 nm compared to P-NiO (1.249 nm), A-NiO (1.208 nm) and B-NiO (0.978 nm). Furthermore, compare to the high RMS roughness value of bare ITO substrate (1.488 nm) shown in **Figure 2-5**, S-NiO film (0.963 nm) clearly planarized the rough surface of ITO and formed highly smooth and uniform film.

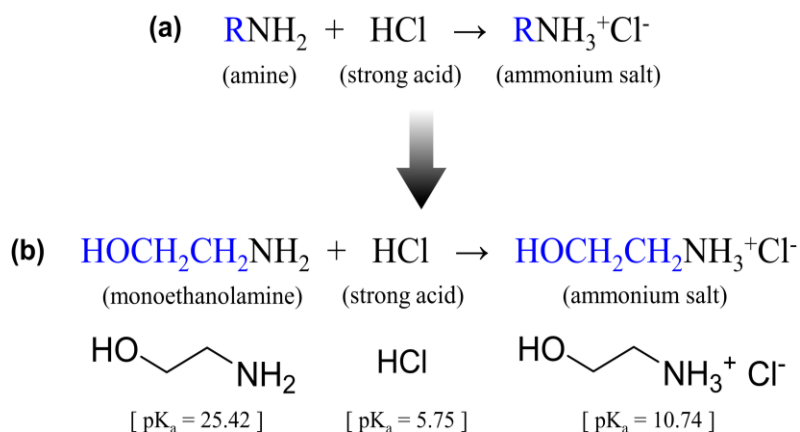


**Figure 2-2.** a) Reaction of amine and strong acid for formation of ammonium salt.  
 b) Reaction of monoethanolamine and hydrochloric acid.

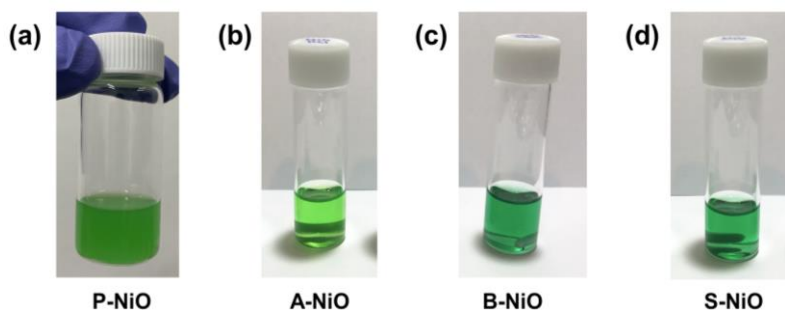


**Figure 2-3.** a) Images of NiO solutions for a) P-NiO, b) A-NiO, c) B-NiO, and d) S-NiO.

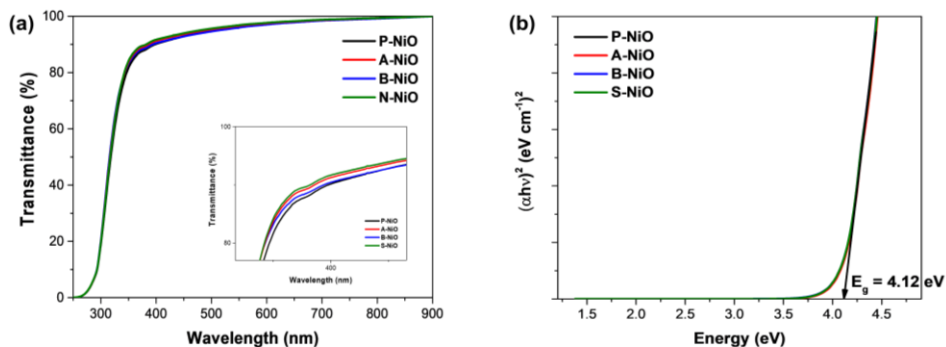


**Figure 2-4.** Optical properties of NiO thin films. a) Ultraviolet-visible transmittance spectra of NiO films with different stabilizer conditions. Inset: enlarged transmittance spectra region between 320 ~ 470 nm. b) Tauc plots of different NiO thin films to determine optical bandgap.

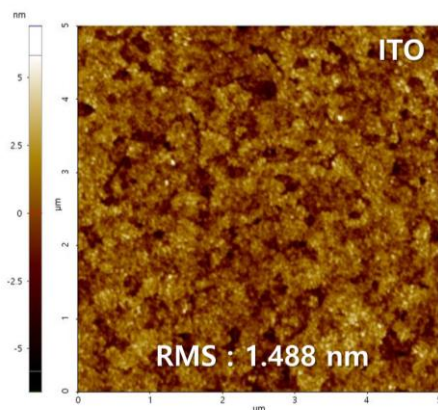


**Figure 2-5.** Atomic force microscopy images of bare ITO substrate in an area of 5 μm × 5 μm. RMS is the root mean square roughness of the film.

Grazing-incidence X-ray diffraction (GI-XRD) was performed to investigate differences in crystal structure of NiO films shown in **Figure 2-6 and Table 2-1**. All NiO films depicted three strong peaks at  $37.2^\circ$ ,  $43.2^\circ$  and  $62.8^\circ$  for  $2\theta$  values which are characteristic peaks for (111), (200), and (220) crystallographic planes of cubic structured NiO.<sup>[15]</sup> This reveals clear formation of NiO films for all three types of NiO with cubic octahedral structure. When we compare the crystallinity of the three NiO films with the same thickness of 20 nm, S-NiO demonstrated stronger intensity and smallest full width at half maximum (FWHM) for all three (111), (200), and (200) peaks (1.022, 1.148, 1.156) which explains enhanced crystallinity compared to A-NiO (1.175, 1.191, 1.287) and B-NiO (1.097, 1.275, 1.249). The results are also in accordance with the results shown from the SEM and AFM images. From these results, it is evident that ammonium salt stabilizer has noticeable impact on NiO's optical and morphological properties. These enhancements in optical and morphological property of NiO can be attributed to the different chelating characteristics of the stabilizers in NiO solution.



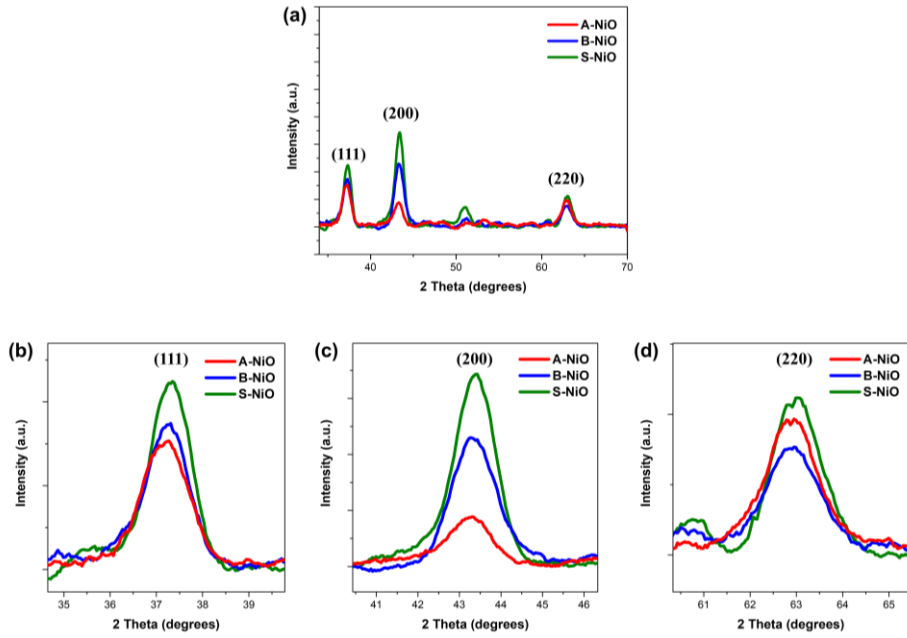


**Figure 2-6.** Comparison of grazing incidence X-ray diffraction patterns of different NiO films with 20 nm thickness. a) full XRD patterns and magnified XRD patterns that belongs to b) (111) plane peak, c) (200) plane peak and d) (220) plane peak.

Peak	A-NiO	B-NiO	S-NiO
(111)	1.175	1.097	1.022
(200)	1.191	1.275	1.148
(220)	1.287	1.249	1.156

**Table 2-1.** Full width at half maximum (FWHM) of ITO/NiO with different stabilizer conditions at different peaks.

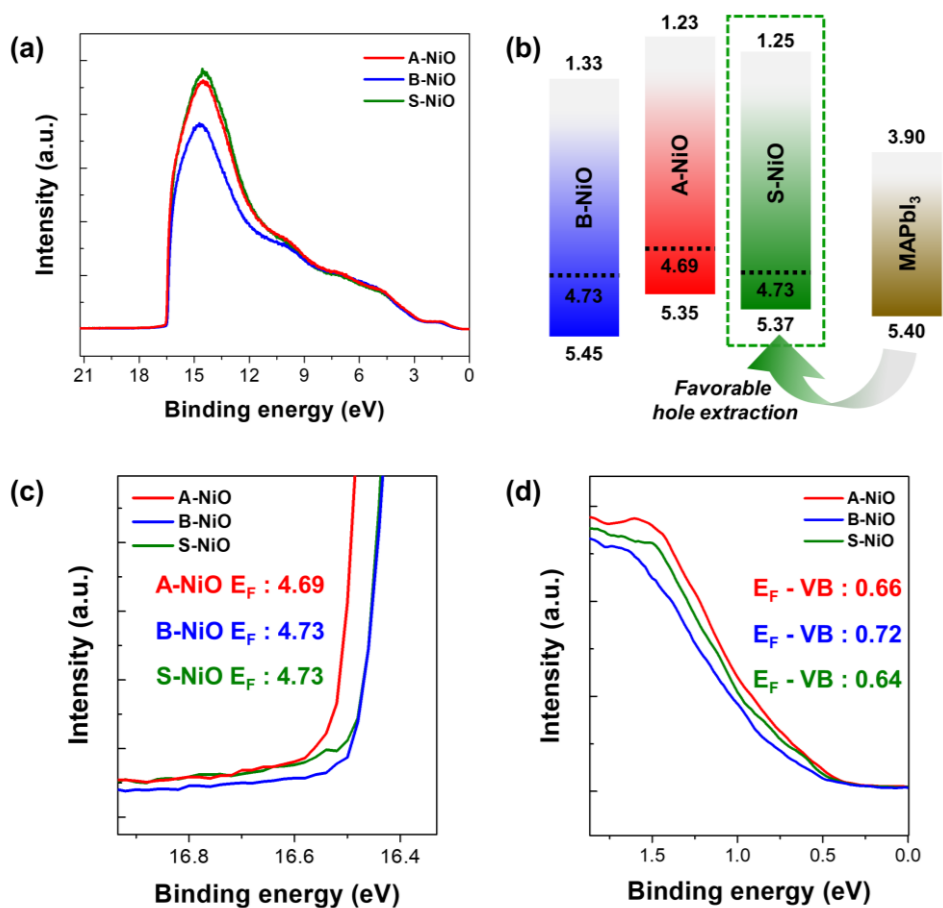


**Figure 2-7.** Ultraviolet photoelectron spectroscopy (UPS) spectra of various NiO films. a) full UPS spectra and UPS spectra in the b) cutoff ( $E_{\text{cutoff}}$ ) energy regions and the c) onset ( $E_{\text{onset}}$ ) regions. d) Detailed energy diagram of different NiO and MAPbI<sub>3</sub>.

To further examine the effect of stabilizers on electronic properties of NiO, we utilized ultraviolet photoelectron spectroscopy (UPS) to probe energy band structure of each NiO thin films. The detailed band diagram is shown in **Figure 2-7** with optical bandgaps ( $E_g$ ) measured using Tauc plots to be approximately  $\sim 4.12$  eV (Figure 2-4b).

Fermi level ( $E_f$ ) was calculated by subtracting secondary energy cutoffs from the excitation energy ( $E_f = h\nu (21.22 \text{ eV}) - E_{cut-off}$ ) and valence band (VB) was measured by calculating the difference between VB and  $E_f$  at the onset region. For p-type semiconductor, the smaller energy gap between the VB and  $E_f$  indicates stronger p-type property and higher hole concentration with the following equation.<sup>[16]</sup>

$$n_p = N_{NiO} e^{\frac{E_f - E_{VBM}}{k_B T}}$$

The calculated  $E_f$  of A-NiO, B-NiO and S-NiO were 4.68, 4.73 and 4.73 eV, and the VB energy levels of A-NiO, B-NiO and S-NiO were measured to be 5.35, 5.45 and 5.37 eV respectively. All NiO demonstrated deep valence band that matches well with the VB of MAPbI<sub>3</sub> (5.4 eV). Notably, S-NiO exhibited the smallest VB –  $E_f$  gap (0.64 eV) compared to A-NiO (0.66 eV) and B-NiO (0.73 eV), which indicates the strongest p-type property and highest hole concentration. Furthermore, with the smallest VB offset to that of perovskite, we can expect improved hole transport from the perovskite layer to S-NiO, which can contribute to higher open circuit voltage ( $V_{oc}$ ).

We fabricated hole-only devices with configuration of ITO/NiO/Au to compare hole transport capability. In **Figure 2-8**, at the same forward bias, S-NiO exhibits

steeper slope and higher current density than P-NiO, A-NiO and B-NiO which implies improved hole conductivity and hole extraction capability.<sup>[8g]</sup>

X-ray photoelectron spectroscopy (XPS) measurement was carried out to investigate hole conductivity. The hole conductivity of NiO originates from  $\text{Ni}^{3+}$  states induced by  $\text{Ni}^{2+}$  vacancies. Typically, higher  $\text{Ni}^{3+} / \text{Ni}^{2+}$  ratio indicates higher hole concentration and hole conductivity of NiO.<sup>[17]</sup> **Figure 2-9** illustrates XPS spectra of Ni  $2p_{3/2}$  and O 1s core levels for different NiO films. Characteristic peaks of  $\text{Ni}^{2+}$  and  $\text{Ni}^{3+}$  are clearly observed in both Ni  $2p_{3/2}$  and O 1s spectrum and the respective area and ratio were calculated in **Table 2-2**. In both spectrum, S-NiO exhibited the highest  $\text{Ni}^{3+} / \text{Ni}^{2+}$  ratio of 1.25 and 0.98 for Ni  $2p_{3/2}$  and O 1s orbitals respectively which delineates higher hole concentration and enhanced hole transport capability than A-NiO (1.16 and 0.73) and B-NiO (1.06 and 0.64). These findings are consistent with the highest hole concentration and highest hole conductivity confirmed by UPS ( $E_f - E_{\text{VBM}}$ ) and hole-only devices respectively.

In order to identify the specific changes in chemical composition of NiO films originating from different stabilizers, we performed depth profiling of ITO/NiO/MAPbI<sub>3</sub> samples using time-of-flight secondary-ion mass spectrometry (ToF-SIMS) under negative polarity as shown in **Figure 2-10**. The  $\text{PbI}_3^-$ ,  $\text{NiO}^-$  and  $\text{InO}^-$  signals represents perovskite, NiO, and ITO layer, respectively. Between the diminishment of  $\text{PbI}_3^-$  peak and the rise of  $\text{InO}^-$  peak, S-NiO demonstrated higher intensity for  $\text{NiN}^-$ ,  $\text{NiCl}^-$ ,  $\text{PbN}^-$  and  $\text{PbCl}^-$  signals than that in P-NiO, A-NiO and B-NiO. The N and Cl bonding with Ni and Pb verifies existence and coordination of ammonium salt at the interface between S-NiO and perovskite layer. Stronger intensity of these peaks indicate stronger bonding and interaction between the layers

which can assist in formation of more robust and smooth interface between NiO and MAPbI<sub>3</sub>. Furthermore, the CN<sup>-</sup> signal between PbI<sub>3</sub><sup>-</sup> and InO<sup>-</sup> peaks exhibit particularly higher intensity in S-NiO sample compared to P-NiO, A-NiO and B-NiO. This possibly delineates constructive interaction of methylammonium and ammonium salt both containing CN bonding.

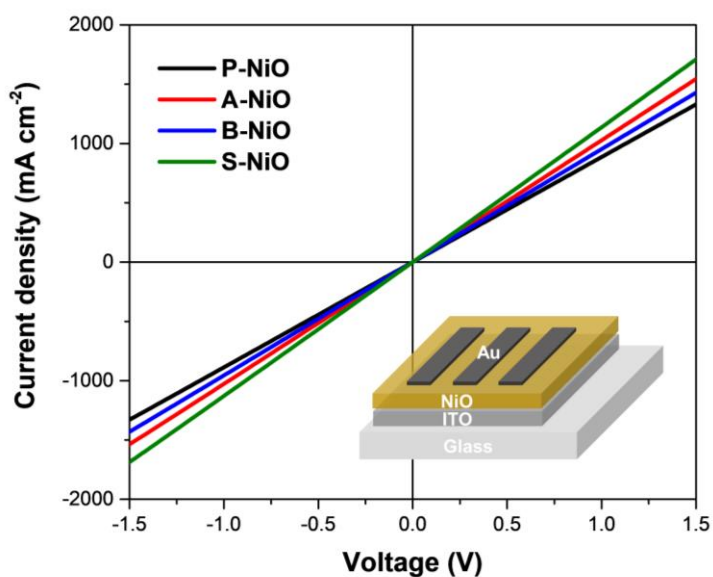


**Figure 2-8.**  $J$ - $V$  curves of hole only devices based on different NiO. The device structure is ITO / NiO / Au.

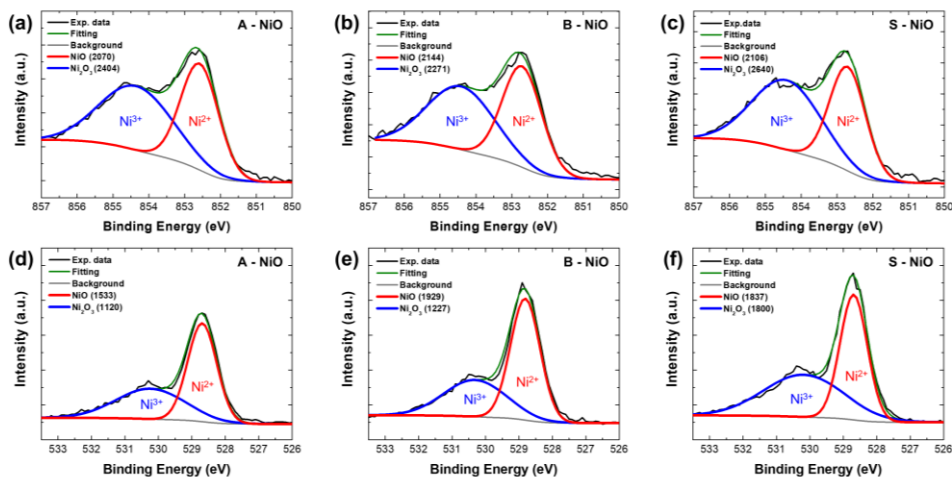


**Figure 2-9.** X-ray photoelectron spectroscopy (XPS) spectra of NiO films with different stabilizers. Ni  $2p_{3/2}$  orbital of a) A-NiO, b) B-NiO, c) S-NiO, and O 1s orbital of d) A-NiO, e) B-NiO, f) S-NiO. The values in bracket resembles the area of deconvoluted peak.

$\text{Ni}^{3+} / \text{Ni}^{2+}$	A-NiO	B-NiO	S-NiO
Ni $2p_{3/2}$	1.16	1.06	1.25
O 1s	0.73	0.64	0.98

**Table 2-2.** Calculated  $\text{Ni}^{3+} / \text{Ni}^{2+}$  ratio for each NiO films in Ni  $2p_{3/2}$  and O 1s orbital. The ratio was calculated by using respective area of deconvoluted peak from XPS data shown in bracket.

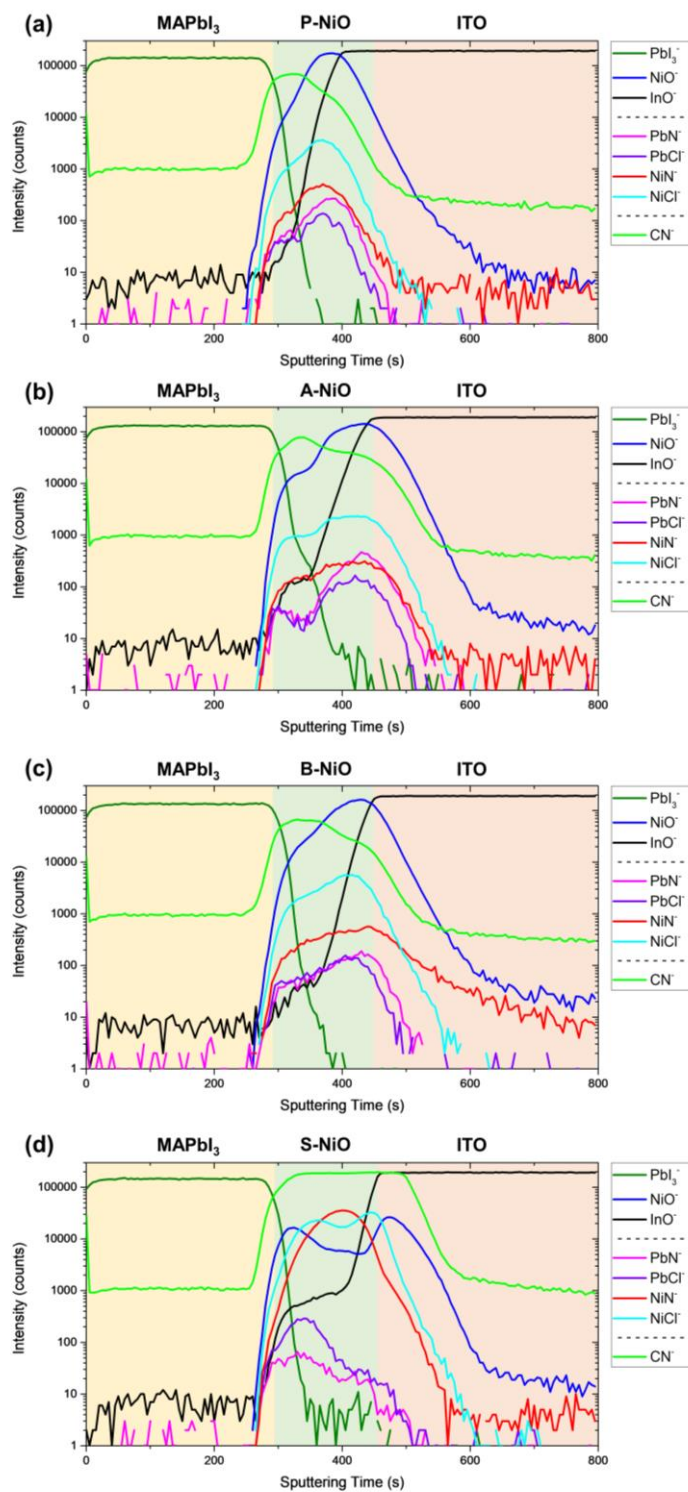


**Figure 2-10.** TOF-SIMS depth profiles measured in negative polarity of ITO/NiO/MAPbI<sub>3</sub> film. a) P-NiO, b) A-NiO, c) B-NiO, and d) S-NiO.

**Figure 2-11a and Table 2-3** present  $J-V$  characteristics of PSC devices based on inverted p-i-n structure of ITO/NiO/MAPbI<sub>3</sub>/PCBM/ZnO/Al. The cross section image and the lateral structure of fabricated device obtained by scanning transmission electron microscopy (STEM) is shown in **Figure 2-12**. As expected, the PSC employing PEDOT:PSS as HTM resulted in low PCE of 12.39% with very low  $V_{oc}$  and  $J_{sc}$  ( 0.96 V, 15.92 mA cm<sup>-2</sup>, 0.81 ) due to its shallow energy level. Then, the PSC with P-NiO as HTM was fabricated and it also exhibited low PCE of 13.20% with low FF ( 1.05 V, 19.56 mA cm<sup>-2</sup>, 0.64 ) due to its poor solubility and rough morphology as we observed in SEM and AFM measurements. On the other hand, the PSC based on NiO with stabilizers demonstrated significant enhancement in PCE. Our reference PSCs with A-NiO and B-NiO exhibited similar PCE of 18.30% ( 1.11 V, 21.70 mA cm<sup>-2</sup>, 0.76 ) and 18.49% ( 1.12 V, 22.00 mA/cm<sup>-2</sup>, 0.75 ) respectively. For the case of S-NiO, however, PSC exhibited even higher PCE of 19.91% ( 1.13 V, 22.56 mA cm<sup>-2</sup>, 0.78 ) with great increase in  $V_{oc}$  and FF even compared to the reference PSCs. These improvements can be ascribed to favorable energy level and improved p-type property of S-NiO which can lead to enhancement in hole extraction. To the best of our knowledge, this is one of the highest PCE and  $V_{oc}$  among the reported MAPbI<sub>3</sub>-based PSCs to date.

The external quantum efficiency (EQE) spectra and integrated current density of PSCs based on different NiO are shown in **Figure 2-13**. The integrated current density of different NiO based PSCs derived from the EQE spectra demonstrates consistency with the  $J_{sc}$  obtained by  $J-V$  curves. In both results, S-NiO based PSCs exhibited higher  $J_{sc}$  and integrated current density (21.6 mA cm<sup>-2</sup>) than that of P-NiO (19.1 mA cm<sup>-2</sup>), A-NiO (20.4 mA cm<sup>-2</sup>), and B-NiO (21.2 mA cm<sup>-2</sup>). Figure 4b, c and



d illustrate  $J-V$  curves of PSCs depending on different scan directions. PSCs with S-NiO exhibited negligible hysteresis with smaller hysteresis index (HI) of 0.029 compared to that of A-NiO (0.068) and B-NiO (0.046). Furthermore, we plotted distribution graphs of PCE and each photovoltaic parameter ( $V_{oc}$ ,  $J_{sc}$  and FF) for 30 different PSC devices based on each NiO (**Figure 2-14 and 2-15**). S-NiO based PSCs demonstrated the narrowest distribution curve at higher value for PCE and all photovoltaic parameters compared to A-NiO and B-NiO. Matching integrated current density, negligible hysteresis and narrow distribution graphs for S-NiO based PSCs indicate high reproducibility and reliability of our strategy, and clearly demonstrate improvement in photovoltaic performance using S-NiO.

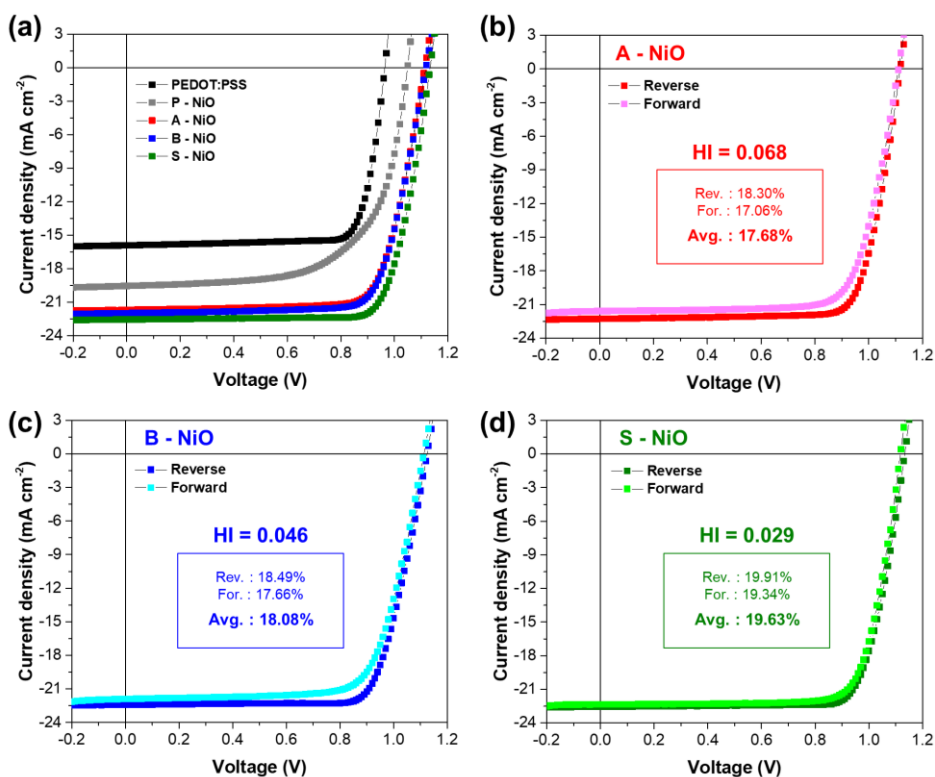


**Figure 2-11.** a) Optimized  $J$ - $V$  curves of PSC devices based on different HTM.  $J$ - $V$  curve of PSC under forward and reverse sweep direction with b) A-NiO c) B-NiO d) S-NiO.

HTM	$V_{oc}$ [V]	$J_{sc}$ [ $\text{mA cm}^{-2}$ ]	FF	PCE
PEDOT:PSS	0.96	15.92	0.81	12.39
P-NiO	1.05	19.56	0.64	13.20
A-NiO	1.11	21.70	0.76	18.30
B-NiO	1.12	22.00	0.75	18.49
S-NiO	1.13	22.56	0.78	19.91

**Table 2-3.** Device parameters of the PSCs based on different HTM. The device parameters of PEDOT:PSS based device are also provided for comparison. Results are extracted from  $J$ - $V$  measurements under standard AM 1.5 illumination ( $100 \text{ mW cm}^{-2}$ ).

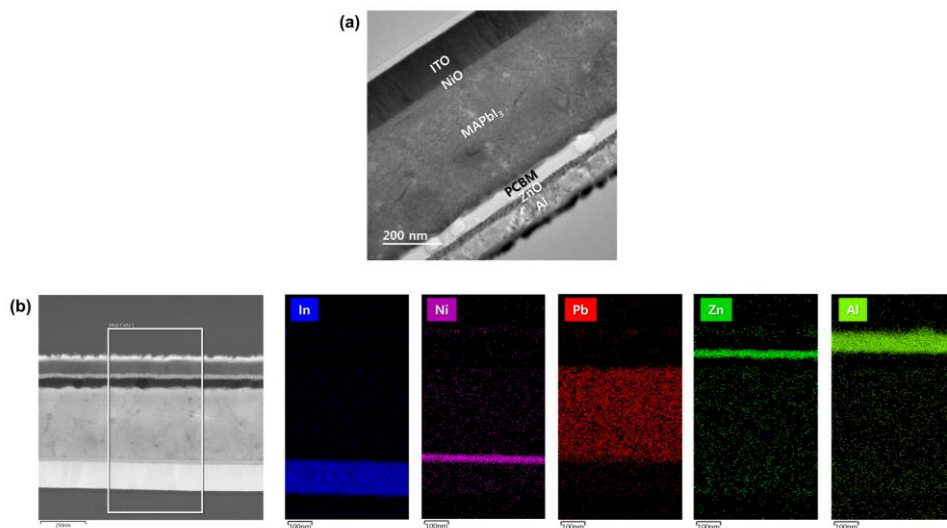


**Figure 2-12.** a) Scanning transmission electron microscopy image of the fabricated PSC device. b) The corresponding element dispersive spectroscopy (EDS) mapping of the lateral structure of PSCs.

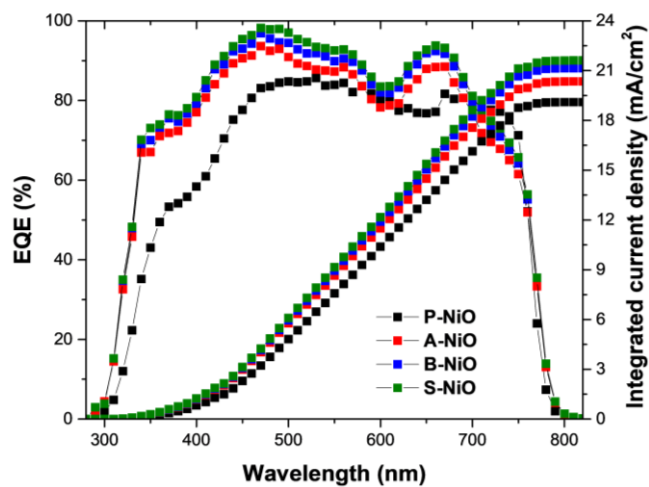


**Figure 2-13.** EQE spectra and integrated current density of perovskite solar cells based on different NiO.

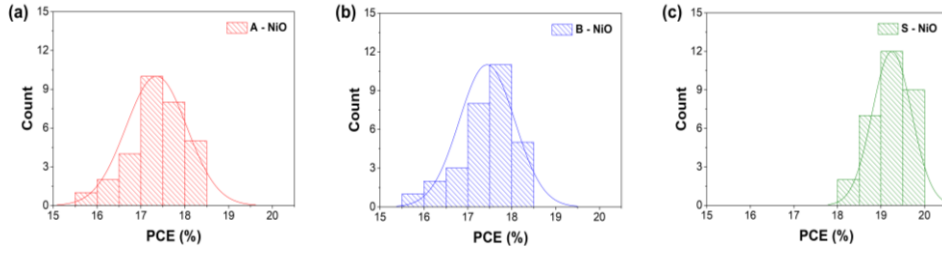


**Figure 2-14.** The PCE distribution graph of PCE for 30 PSC devices based on a) A-NiO, b) B-NiO and c) S-NiO.

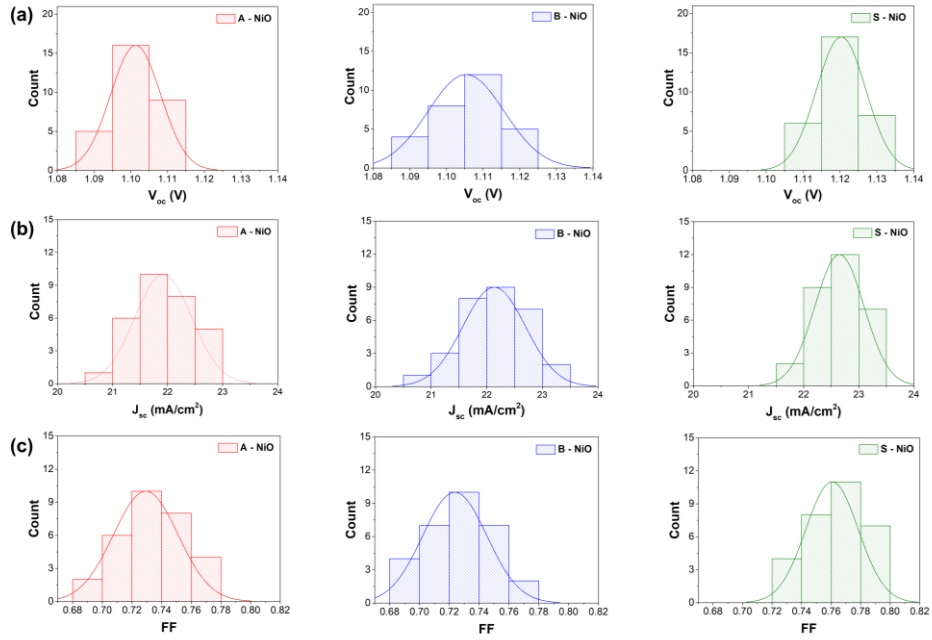


**Figure 2-15.** The distribution graph for different photovoltaic parameters a)  $V_{oc}$ , b)  $J_{sc}$ , and c) FF for 30 PSC devices based on different NiO.

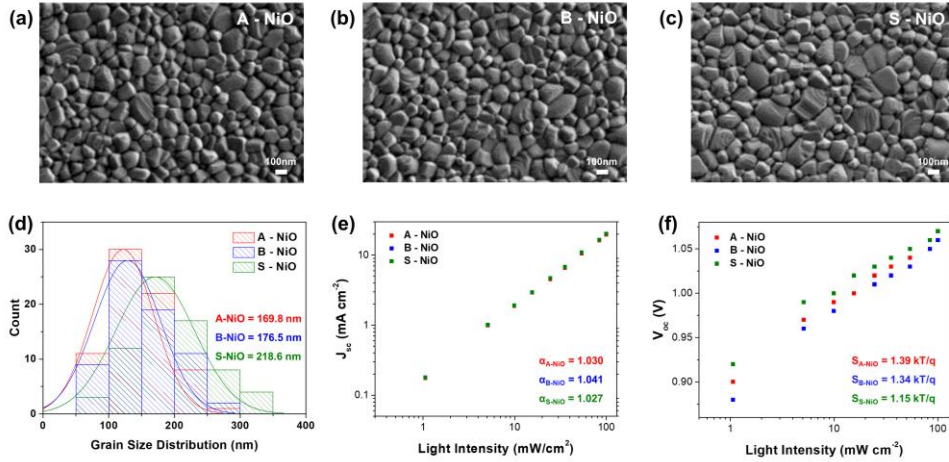


**Figure 2-16.** Top-view scanning electron microscopy (SEM) images of MAPbI<sub>3</sub> perovskite films on top of a) A-NiO, b) B-NiO, and c) S-NiO at 50K magnification. d) Grain size distribution of perovskite films on different NiO. e)  $J_{sc}$  and f)  $V_{oc}$  values of PSCs with different NiO as function of light illumination intensity.

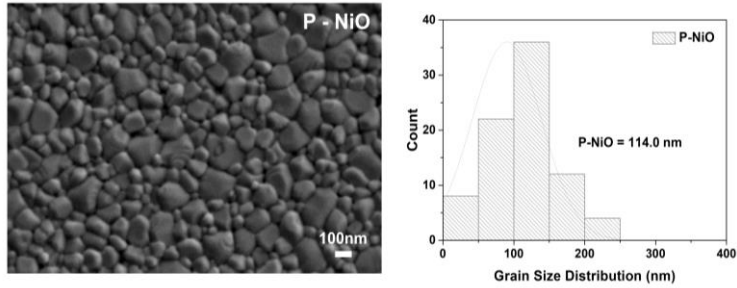


**Figure 2-17.** a) Top-view scanning electron microscopy (SEM) image of MAPbI<sub>3</sub> perovskite film on top of P-NiO. b) Grain size distribution of perovskite films on P-NiO.

To further understand the origin of the enhancement in photovoltaic parameters, we investigated the interface between perovskite and NiO and also the quality of perovskite film. Due to the possible influence of underlying NiO film on the formation of perovskite film atop, we first evaluated perovskite film morphology. **Figure 2-16a, b, c, d and 2-17** show SEM images of MAPbI<sub>3</sub> film on different NiO films and their grain size distribution. Perovskite film varied depending on the underlying HTM by demonstrating larger average grain size (218.6 nm) on top of S-NiO than that of P-NiO (114.0 nm), A-NiO (169.8 nm) and B-NiO (176.5 nm).<sup>[18]</sup>

We then studied wettability of MAPbI<sub>3</sub> solution on HTM. The solution wettability on the HTM is of significance due to its impact on the grain size and film formation of perovskite layer. **Figure 2-18** summarizes the contact angle of MAPbI<sub>3</sub> solution droplet on NiO thin films with different stabilizer conditions. S-NiO exhibited the most hydrophilic surface with the smallest contact angle of 42.76° compared to the others (48.37° for P-NiO, 47.32° for A-NiO, and 43.62° for B-NiO). The reason for the smaller contact angle of S-NiO than P-NiO, A-NiO and B-NiO can be attributed to the obtained results from TOF-SIMS where existence of ammonium salt at the interface between S-NiO and MAPbI<sub>3</sub> brought constructive interaction shown by the increase in PbN<sup>+</sup>, PbCl<sup>+</sup> and CN<sup>+</sup> peak. As a result, perovskite film on top of S-NiO showed the biggest average grain size. The enhanced perovskite film quality with larger grain size and better coverage can effectively suppress unfavorable charge recombination and facilitate efficient charge transport.

We looked into the charge carrier recombination features within the device by measuring light intensity dependence of  $J_{sc}$  and  $V_{oc}$  as shown in Figure 5e and f.  $J_{sc}$  as a function of light intensity should follow power law dependence formula ( $J \approx I^\alpha$ ).

$\alpha$  will equal to 1 for an ideal system with no bimolecular recombination.<sup>[19]</sup> The  $\alpha$  values of PSC devices using A-NiO, B-NiO and S-NiO are 1.03, 1.04 and 1.02 respectively. The trivial difference in  $\alpha$  values for all NiO based PSC devices elucidate negligible bimolecular recombination in PSC devices.

For the light intensity dependence of  $V_{oc}$ , we measured the slope of the device  $\approx \frac{k_B T}{q}$  (where  $k_B$  is Boltzmann constant, T is absolute temperature, and q is elementary charge). It has been reported that a trap-free relationship will have a slope of  $1 \frac{k_B T}{q}$ , whereas trap-assisted recombination will have a slope greater than  $1 \frac{k_B T}{q}$ .<sup>[20]</sup> PSC devices based on A-NiO, B-NiO, and S-NiO exhibited different slope values of be 1.39, 1.34 and  $1.15 \frac{k_B T}{q}$  respectively. The distinct difference in the slope values suggests that trap-assisted recombination is the dominant mechanism. Furthermore, larger slope values for A-NiO and B-NiO indicate that they suffer more from trap-assisted recombination than S-NiO. Reduced trap-assisted recombination for S-NiO demonstrate reduced defects and improved interface quality resulting in efficient charge collection at the anode, which must have contributed to the enhanced performance, especially with higher  $V_{oc}$  and FF for S-NiO based PSC devices.

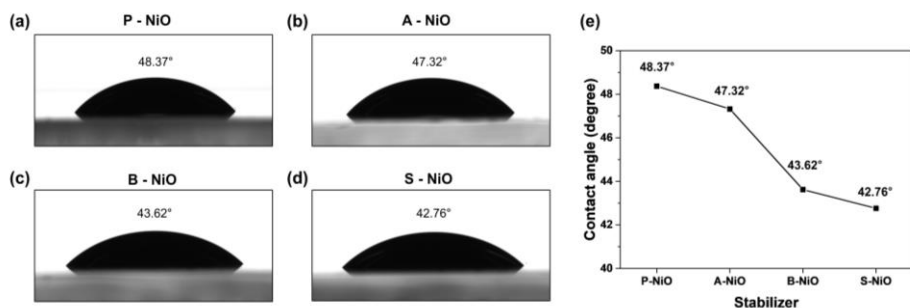


**Figure 2-18.** Contact angle of MAPbI<sub>3</sub> solution droplet on different NiO films. a) P-NiO, b) A-NiO, c) B-NiO and d) S-NiO, and e) results plotted on a graph.

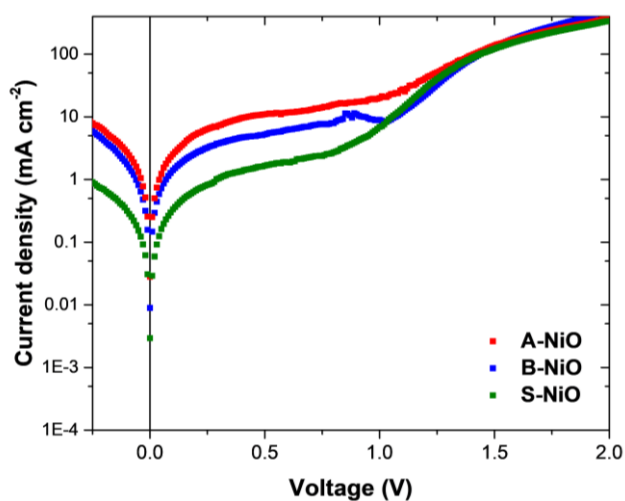


**Figure 2-19.** Dark  $J$ - $V$  characteristics of PSC devices based on different NiO.



In addition, from the dark  $J$ – $V$  characteristics of PSC shown in **Figure 2-19**, at the reverse bias region, PSCs based on S-NiO demonstrate smaller leakage current than A-NiO and B-NiO. Reduced leakage current at the dark indicates higher shunt resistance and reduced charge recombination, which results in higher FF. Moreover, the steeper slope of S-NiO at forward bias delineates lower series resistance compared to others. These results are in good agreement with the  $J$ – $V$  performances and light intensity experiments, where S-NiO based PSCs exhibited higher  $V_{oc}$  and FF attributed to reduced charge recombination.

**Figure 2-20** shows pH values of different NiO solutions measured with pH paper and pH meter. Depending on the stabilizer used in NiO, we could observe a clear modulation of pH value of NiO solution. A-NiO exhibited an acidic pH of 4.81, whereas B-NiO showed an alkaline pH of 9.84. In contrast, S-NiO demonstrated relatively neutral pH value of 7.21. We suppose the reduced trap assisted recombination in S-NiO is most likely related to this quasi-neutral nature of ammonium salt stabilizer.

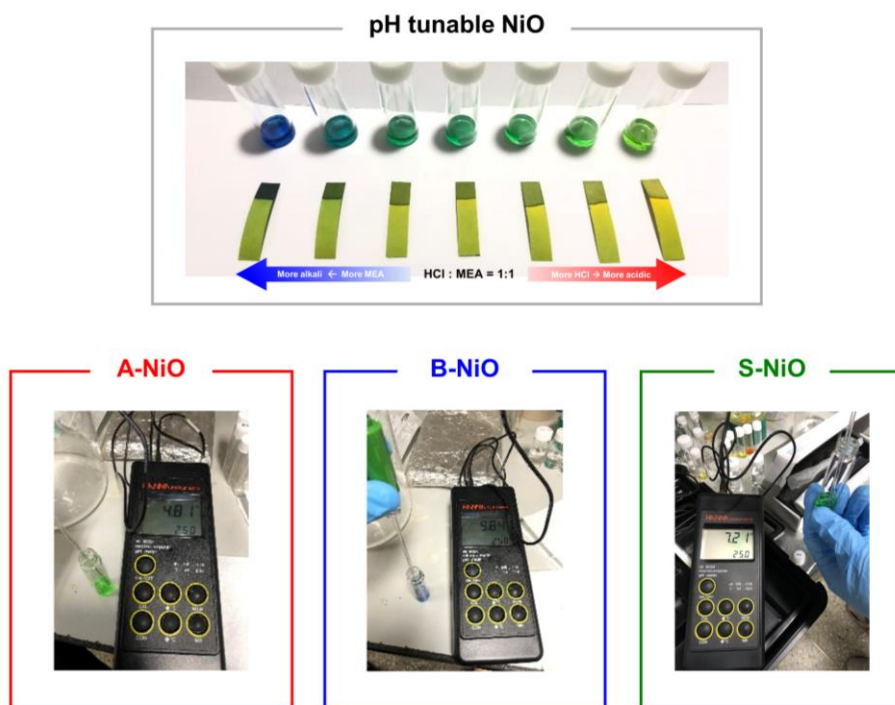


**Figure 2-20.** Images of different NiO solution with varying stabilizer conditions and its pH value measured by pH paper and pH meter.

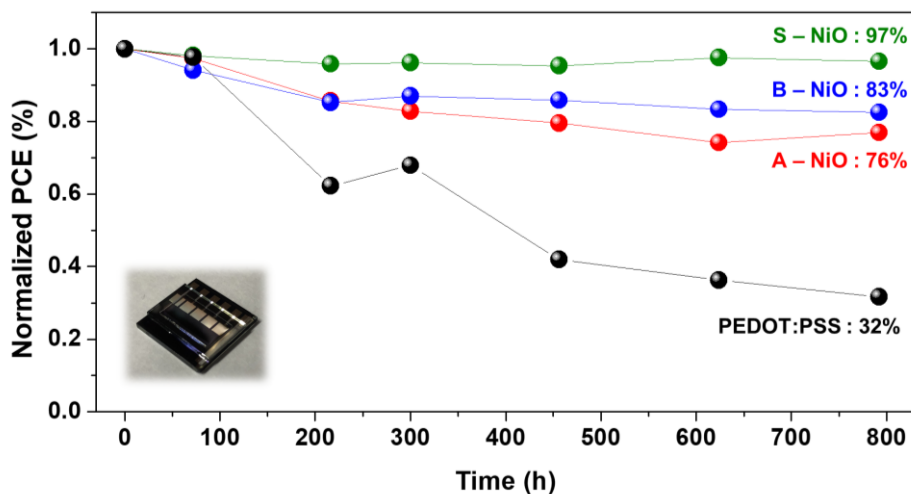


**Figure 2-21.** Air stability of encapsulated devices based on different hole transporting materials. The inset shows the corresponding image of perovskite solar cell devices with glass encapsulation.

We monitored the performance of PSC devices with encapsulation for 800 h under ambient atmosphere at relative humidity (RH) of  $40\pm5\%$  as shown in **Figure 2-21**. Encapsulating glass covered the active area of PSC devices from the top and UV resin was used as adhesion. We encapsulated the PSC device (inset image of Figure 6) to focus on the interface between HTM and perovskite layer. PEDOT:PSS based PSC devices demonstrated poor device stability by maintaining only 32% of its initial performance. While PSC devices with A-NiO and B-NiO preserved only 76% and 83% of its initial PCE, PSC devices with S-NiO exhibited superior stability and maintained more than 97% of its original efficiency. As expected, S-NiO with ammonium salt stabilizer with comparably more neutral pH, demonstrated highest device stability.

## 2.4 Conclusion and outlook

To summarize, we have successfully demonstrated highly efficient and stable PSCs employing an ammonium salt based sol-gel NiO. By using ammonium salt, we were able to fabricate more smooth and crystalline NiO film and thus achieve improved morphology and higher crystallinity. Furthermore, interfacial properties, energy level and hole conductivity were modulated to improve hole transportation between NiO and perovskite layer. These modifications as a result led to enhanced device performance by achieving high  $V_{oc}$  (1.13V) and FF(0.78) and minimized trap-assisted recombination. The optimized device exhibited PCE of 19.91%. In addition, the relatively more neutral pH of NiO solution ensured robust device lifetime maintaining more than 97% of its initial PCE for 800 h with encapsulation. We expect that our result will provide a new direction for highly efficient and stable p-i-n based PSCs.

## 2.5 Bibliography

- [1] A. Kojima, K. Teshima, Y. Shirai, T. Miyasaka, *J. Am. Chem. Soc.* **2009**, *131*, 6050.
- [2] a) O. Malinkiewicz, A. Yella, Y. H. Lee, G. M. Espallargas, M. Graetzel, M. K. Nazeeruddin, H. J. Bolink, *Nat. Photonics* **2014**, *8*, 128; b) S. D. Stranks, G. E. Eperon, G. Grancini, C. Menelaou, M. J. P. Alcocer, T. Leijtens, L. M. Herz, A. Petrozza, H. J. Snaith, *Science* **2013**, *342*, 341; c) J. H. Noh, S. H. Im, J. H. Heo, T. N. Mandal, S. I. Seok, *Nano Lett.* **2013**, *13*, 1764.
- [3] a) X. Yin, P. Chen, M. Que, Y. Xing, W. Que, C. Niu, J. Shao, *ACS Nano* **2016**, *10*, 3630; b) M. P. de Jong, L. J. van Ijzendoorn, M. J. A. de Voigt, *Appl. Phys. Lett.* **2000**, *77*, 2255; c) M. Jørgensen, K. Norrman, F. C. Krebs, *Sol. Energy Mater Sol. Cells* **2008**, *92*, 686; d) J. Cameron, P. J. Skabara, *Materials Horizons* **2020**, *7*, 1759.
- [4] S. D. Yambem, K.-S. Liao, N. J. Alley, S. A. Curran, *J. Mater. Chem.* **2012**, *22*, 6894.
- [5] a) J.-Y. Jeng, K.-C. Chen, T.-Y. Chiang, P.-Y. Lin, T.-D. Tsai, Y.-C. Chang, T.-F. Guo, P. Chen, T.-C. Wen, Y.-J. Hsu, *Adv. Mater.* **2014**, *26*, 4107; b) M. D. Irwin, D. B. Buchholz, A. W. Hains, R. P. H. Chang, T. J. Marks, *Proc. Natl. Acad. Sci. U.S.A.* **2008**, *105*, 2783; c) K. X. Steirer, P. F. Ndione, N. E. Widjonarko, M. T. Lloyd, J. Meyer, E. L. Ratcliff, A. Kahn, N. R. Armstrong, C. J. Curtis, D. S. Ginley, J. J. Berry, D. C. Olson, *Adv. Energy Mater.* **2011**, *1*, 813.
- [6] a) S. Seo, S. Jeong, C. Bae, N.-G. Park, H. Shin, *Adv. Mater.* **2018**, *30*, 1801010; b) J. H. Park, J. Seo, S. Park, S. S. Shin, Y. C. Kim, N. J. Jeon, H.-W. Shin, T. K. Ahn, J. H. Noh, S. C. Yoon, C. S. Hwang, S. I. Seok, *Adv. Mater.* **2015**, *27*, 4013;

- c) E. Aydin, J. Troughton, M. De Bastiani, E. Ugur, M. Sajjad, A. Alzahrani, M. Neophytou, U. Schwingenschlögl, F. Laquai, D. Baran, S. De Wolf, *ACS Appl. Energy Mater.* **2018**, *1*, 6227; d) Z. Liu, J. Chang, Z. Lin, L. Zhou, Z. Yang, D. Chen, C. Zhang, S. Liu, Y. Hao, *Adv. Energy Mater.* **2018**, *8*, 1703432; e) S. Pang, C. Zhang, H. Dong, D. Chen, W. Zhu, H. Xi, J. Chang, Z. Lin, J. Zhang, Y. Hao, *ACS Appl. Energy Mater.* **2019**, *2*, 4700; f) T. Wang, D. Ding, H. Zheng, X. Wang, J. Wang, H. Liu, W. Shen, *Sol. RRL* **2019**, *3*, 1900045; g) H. Zhang, J. Cheng, F. Lin, H. He, J. Mao, K. S. Wong, A. K. Y. Jen, W. C. H. Choy, *ACS Nano* **2016**, *10*, 1503; h) M. Najafi, F. Di Giacomo, D. Zhang, S. Shanmugam, A. Senes, W. Verhees, A. Hadipour, Y. Galagan, T. Aernouts, S. Veenstra, R. Andriessen, *Small* **2018**, *14*, 1702775; i) Y. Li, W. Sun, F. Gu, D. Ouyang, Z. Bian, Z. Liu, W. C. H. Choy, T. L. Kelly, *Adv. Mater. Interfaces* **2019**, *6*, 1900474.
- [7] a) J. Ciro, D. Ramírez, M. A. Mejía Escobar, J. F. Montoya, S. Mesa, R. Betancur, F. Jaramillo, *ACS Appl. Mater. Interfaces* **2017**, *9*, 12348; b) J. He, E. Bi, W. Tang, Y. Wang, Z. Zhou, X. Yang, H. Chen, L. Han, *Sol. RRL* **2018**, *2*, 1800004; c) S. Y. Park, S. J. Kim, J. H. Lee, M. J. Jeong, J. M. Lee, H. S. Jung, J. H. Noh, *Adv. Funct. Mater.* **2021**, *31*, 2100863; d) W. Chen, Y. Wu, J. Fan, A. B. Djurišić, F. Liu, H. W. Tam, A. Ng, C. Surya, W. K. Chan, D. Wang, Z.-B. He, *Adv. Energy Mater.* **2018**, *8*, 1703519.
- [8] a) J. H. Kim, P.-W. Liang, S. T. Williams, N. Cho, C.-C. Chueh, M. S. Glaz, D. S. Ginger, A. K. Y. Jen, *Adv. Mater.* **2015**, *27*, 695; b) W. Nie, H. Tsai, J.-C. Blancon, F. Liu, C. C. Stoumpos, B. Traore, M. Kepenekian, O. Durand, C. Katan, S. Tretiak, J. Crochet, P. M. Ajayan, M. Kanatzidis, J. Even, A. D. Mohite, *Adv. Mater.* **2018**, *30*, 1703879; c) W. Chen, Y. Wu, Y. Yue, J. Liu, W. Zhang, X. Yang,

- H. Chen, E. Bi, I. Ashraful, M. Grätzel, L. Han, *Science* **2015**, *350*, 944; d) Y. Xie, K. Lu, J. Duan, Y. Jiang, L. Hu, T. Liu, Y. Zhou, B. Hu, *ACS Appl. Mater. Interfaces* **2018**, *10*, 14153; e) B. Ge, H. W. Qiao, Z. Q. Lin, Z. R. Zhou, A. P. Chen, S. Yang, Y. Hou, H. G. Yang, *Sol. RRL* **2019**, *3*, 1900192; f) S. Teo, Z. Guo, Z. Xu, C. Zhang, Y. Kamata, S. Hayase, T. Ma, *ChemSusChem* **2019**, *12*, 518; g) W. Chen, F.-Z. Liu, X.-Y. Feng, A. B. Djurišić, W. K. Chan, Z.-B. He, *Adv. Energy Mater.* **2017**, *7*, 1700722.
- [9] a) W. Chen, Y. Zhou, L. Wang, Y. Wu, B. Tu, B. Yu, F. Liu, H.-W. Tam, G. Wang, A. B. Djurišić, L. Huang, Z. He, *Adv. Mater.* **2018**, *30*, 1800515; b) Q. Wang, C.-C. Chueh, T. Zhao, J. Cheng, M. Eslamian, W. C. H. Choy, A. K. Y. Jen, *ChemSusChem* **2017**, *10*, 3794; c) X. Li, X. Zhao, F. Hao, X. Yin, Z. Yao, Y. Zhou, H. Shen, H. Lin, *ACS Appl. Mater. Interfaces* **2018**, *10*, 17861.
- [10] a) C. C. Boyd, R. C. Shallcross, T. Moot, R. Kerner, L. Bertoluzzi, A. Onno, S. Kavadiya, C. Chosy, E. J. Wolf, J. Werner, J. A. Raiford, C. de Paula, A. F. Palmstrom, Z. J. Yu, J. J. Berry, S. F. Bent, Z. C. Holman, J. M. Luther, E. L. Ratcliff, N. R. Armstrong, M. D. McGehee, *Joule* **2020**, *4*, 1759; b) Y. Guo, J. Ma, H. Wang, F. Ye, L. Xiong, H. Lei, Z. Tan, *Adv. Mater. Interfaces* **2021**, *8*, 2100920.
- [11] a) C. Hu, Y. Bai, S. Xiao, K. Tao, W. K. Ng, K. S. Wong, S. H. Cheung, S. K. So, Q. Chen, S. Yang, *Sol. RRL* **2020**, *4*, 2000270; b) R. Wang, M. Mujahid, Y. Duan, Z.-K. Wang, J. Xue, Y. Yang, *Adv. Funct. Mater.* **2019**, *29*, 1808843.
- [12] a) A. T. Gidey, D.-W. Kuo, A. D. Fenta, C.-T. Chen, C.-T. Chen, *ACS Appl. Energy Mater.* **2021**, *4*, 6486; b) B. G. Kim, W. Jang, Y. J. Park, J. H. Kang, J. H. Seo, D. H. Wang, *J. Phys. Chem. C* **2020**, *124*, 25184.

- [13] a) M. Yi, W. Jang, D. H. Wang, *ACS Sustainable Chemistry & Engineering* **2019**, 7, 8245; b) N. K. Noel, M. Congiu, A. J. Ramadan, S. Fearn, D. P. McMeekin, J. B. Patel, M. B. Johnston, B. Wenger, H. J. Snaith, *Joule* **2017**, 1, 328; c) J. J. Yoo, G. Seo, M. R. Chua, T. G. Park, Y. Lu, F. Rotermund, Y.-K. Kim, C. S. Moon, N. J. Jeon, J.-P. Correa-Baena, V. Bulović, S. S. Shin, M. G. Bawendi, J. Seo, *Nature* **2021**, 590, 587.
- [14] R. J. Ouellette, J. D. Rawn, *23 - Amines and Amides*, Elsevier, Boston **2014**.
- [15] Z. Zhu, Y. Bai, T. Zhang, Z. Liu, X. Long, Z. Wei, Z. Wang, L. Zhang, J. Wang, F. Yan, S. Yang, *Angew. Chem.* **2014**, 126, 12779.
- [16] S. Xiao, F. Xu, Y. Bai, J. Xiao, T. Zhang, C. Hu, X. Meng, H. Tan, H.-P. Ho, S. Yang, *Sol. RRL* **2019**, 3, 1800278.
- [17] a) S. Nandy, B. Saha, M. K. Mitra, K. K. Chattopadhyay, *J. Mater. Sci.* **2007**, 42, 5766; b) C.-C. Wu, C.-F. Yang, *Sol. Energy Mater Sol. Cells* **2015**, 132, 492.
- [18] a) J. H. Lee, Y. W. Noh, I. S. Jin, J. W. Jung, *Electrochim. Acta* **2018**, 284, 253; b) Y. Cheng, Q.-D. Yang, J. Xiao, Q. Xue, H.-W. Li, Z. Guan, H.-L. Yip, S.-W. Tsang, *ACS Appl. Mater. Interfaces* **2015**, 7, 19986; c) H. Guo, X. Huang, B. Pu, J. Yang, H. Chen, Y. Zhou, J. Yang, Y. Li, Z. Wang, X. Niu, *RSC Advances* **2017**, 7, 50410; d) D. Yang, R. Yang, K. Wang, C. Wu, X. Zhu, J. Feng, X. Ren, G. Fang, S. Priya, S. Liu, *Nature Commun.* **2018**, 9, 3239.
- [19] L. J. A. Koster, V. D. Mihailetschi, H. Xie, P. W. M. Blom, *Appl. Phys. Lett.* **2005**, 87, 203502.
- [20] a) M. M. Mandoc, F. B. Kooistra, J. C. Hummelen, B. de Boer, P. W. M. Blom, *Appl. Phys. Lett.* **2007**, 91, 263505; b) J. Vollbrecht, V. V. Brus, S.-J. Ko, J. Lee, A. Karki, D. X. Cao, K. Cho, G. C. Bazan, T.-Q. Nguyen, *Adv. Energy*

*Mater.* **2019**, *9*, 1901438.



# **Chapter 3. Nickel oxide utilizing dipole induced energy level modification for high performance non-fullerene organic solar cells**

## **3.1 Research background**

Over the past few decades, as a potential candidate for next-generation photovoltaics, massive amount of studies have been carried out on organic solar cells (OSCs) due to their advantages of solution processability, low cost and high flexibility.<sup>[1]</sup> Recently, OSCs have shown a dramatic increase in their certified power conversion efficiency (PCE) reaching over 18%.<sup>[2]</sup> This significant advancement is achieved by the development of novel donor and acceptor materials used for bulkheterojunction (BHJ) layer. Especially, the acceptor materials used for BHJ layer have gone through a paradigm shift from wide bandgap, rigid and bulky fullerene based acceptors such as 3D-shaped [6,6]-phenyl C<sub>71</sub> butyric acid methyl ester (PC<sub>71</sub>BM) to low bandgap, easily tunable small molecule non-fullerene acceptors (NFAs) such as 2,2'-((2Z,2'Z)-((12,13-bis(2-ethylhexyl)-3,9-diundecyl-12,13-dihydro-1,2,5]thiadiazolo[3,4-c]thieno[2'',3'':4',5']thieno[2',3':4,5]pyrrolo[3,2-g]thieno[2',3':4,5]thieno[3,2-b]indole-2,10-diyl)bis(methanylylidene))bis(5,6-difluoro-3-oxo-2,3-dihydro-1H-indene-2,1-diylidene))dimalononitrile (Y6).<sup>[3]</sup> This allowed complementary absorption between donor and acceptor materials and also diversity in molecule structure and energy level of acceptors, which resulted in great breakthrough in PCE.<sup>[4]</sup> One of the representative donor-acceptor pair is medium bandgap ( $E_g \sim 1.8$  eV) polymer, poly[(2,6-(4,8-bis(5-(2-ethylhexyl-3-

fluoro)thiophen-2-yl)-benzo[1,2-b:4,5-b']dithiophene))-alt-(5,5-(1',3'-di-2-thienyl-5',7'-bis(2-ethylhexyl)benzo[1',2'-c:4',5'-c']dithiophene-4,8-dione)] (PM6) and low bandgap ( $E_g \sim 1.3$  eV) small molecule acceptor Y6.<sup>[5]</sup>

When using these high-performing donor and acceptor based BHJ, separate charge transporting materials which govern interfacial charge transport and recombination are critical in determining the overall performance of OSC devices.<sup>[6]</sup> To date, poly(3,4-ethylenedioxythiophene):poly(styrenesulfonate) (PEDOT:PSS) is commonly used as HTM due to its high transparency, high conductivity and good film forming property.<sup>[7]</sup> Nevertheless, acidic and hygroscopic nature of PEDOT:PSS is fatal to long-term stability of OSC devices.<sup>[8]</sup> On the other hand, practically more stable inorganic hole transporting materials (HTMs) like nickel oxide (NiO) show rather limited performance according to their energy level mismatch with PM6:Y6 generally leading to high open circuit voltage ( $V_{oc}$ ) loss.

Solution processable metal oxides such as molybdenum oxide ( $\text{MoO}_3$ ), tungsten oxide ( $\text{WO}_3$ ), vanadium oxide ( $\text{V}_2\text{O}_5$ ), and NiO are promising candidates to replace PEDOT:PSS owing to their good charge transporting properties and high stability.<sup>[9]</sup> Kang *et al.* reported the use of ethylene glycol in  $\text{MoO}_x$  to fabricate printable, large-area processable NFA (IT-M) and PB3T based organic solar cells with 12.1%.<sup>[10]</sup> Fu *et al.* reported 11.4% PCE using  $\text{CoO}_x$  as HTM for PBDB-T-2Cl:IT-4F and Alkarsifi *et al.* reported 7.9% PCE utilizing F4-TCNQ doped Cu:NiO as HTM for PM6:IT-4F.<sup>[11]</sup> Recently, Tran *et al.* reported the use of aqueous  $\text{MoO}_x$  and NiO-PTF-BOA for PM6:Y6 system with high PCE of 17.0% and 16.4%.<sup>[12]</sup> However, studies of metal oxides as HTM for recent high performing NFA such as Y6 based OSCs is still limited compared to the counterpart organic HTMs. The limited application of metal

oxide HTMs in NFA based OSCs is mainly due to the mismatch in energy level and also the hetero-interface between inorganic metal oxide and organic active layer.<sup>[13]</sup>

An effective way to reduce energetic barrier between the BHJ and hole transporting layer (HTL) is to manage built-in potential. Increasing the built-in potential can promote charge transport by suppressing unwanted charge accumulation and recombination.<sup>[14]</sup> In order to strengthen this built-in potential, numerous materials with electric dipole moment such as conjugated polyelectrolytes, ferroelectric polymers and self-assemble monolayers have been adopted.<sup>[15]</sup> These materials generate interfacial dipoles which modify work function (WF) and alleviate energetic barrier. However, until now, successful use of interfacial dipoles for p-type metal oxide to maximize its hole transporting ability for high performance NFA OSCs is lacking.<sup>[16]</sup>

In this study, we utilize potassium and sodium salts of hydroquinone sulfonic acid to fabricate highly efficient NiO based NFA OSCs. Due to the ionic groups in these hydroquinone sulfonic acid (HSA) based salts, these molecules possess dipole moment which induce WF modulation and hole transport enhancement of NiO layer. We applied our modified NiO as HTM for NFA OSCs with PM6 as the donor and 2,2'-((2Z,2'Z)-((12,13-bis(2-butyloctyl)-3,9-diundecyl-12,13-dihydro-[1,2,5]thiadiazolo[3,4-e]thieno[2'',3'':4',5']thieno[2',3':4,5]pyrrolo[3,2-g]thieno[2',3':4,5]thieno[3,2-b]indole-2,10-diyl)bis(methanylylidene))bis(5,6-difluoro-3-oxo-2,3-dihydro-1H-indene-2,1-diylidene))dimalononitrile (Y6-BO-4F) as the acceptor material. Under optimum condition, by using NiO with the addition of HSA based salts, we were able to obtain significant improvement in  $V_{oc}$  from 0.79 V to 0.86 V and achieve high PCE comparable to that of PEDOT:PSS. Furthermore,

OSCs based on NiO with HSA based salts demonstrated superior stability than that of PEDOT:PSS in ambient atmosphere for 1200 h.

## **3.2 Experimental methods**

### **3.2.1 Material preparation**

Nickel acetate tetrahydrate (99.999 %) was purchased from Alfa Aesar and 2-methoxyethanol was purchased from Sigma Aldrich. NiO was prepared according to the previously reported method.<sup>[17]</sup> We fabricated NiO by dissolving 0.05 M of nickel acetate tetrahydrate in 2-methoxyethanol. Hydroquinone sulfonic acid potassium salt and hydroquinone sulfonic acid sodium salt were dissolved in 2-methoxyethanol at 5 mM concentration and added to NiO solution at 1 ~ 10 vol%. For bi-layer structure, 1 ~ 10 mM of hydroquinone sulfonic acid potassium and sodium salt were dissolved in 2-methoxyethanol and spin-coated on top of NiO at 4000 rpm for 30 s, followed by annealing at 80 °C for 10 min.

### **3.2.2 Organic solar cell fabrication**

Patterned ITO glass substrates were cleaned in deionized water, acetone and isopropanol (IPA) respectively, for 15 min, via ultrasonication before use. UV-Ozone was used to treat the substrates for 30 min. For PEDOT:PSS based OSCs, PEDOT:PSS (Clevios P VP AI 4083) solution was spin-coated on these cleaned substrates at the speed of 5000 rpm for 30 s, followed by annealing at 150 °C for 15 min. For NiO based OSCs, NiO solution was spin-coated at the speed of 6000 rpm for 30 s, followed by annealing at 300 °C for 30 min. BHJ solution was obtained by dissolving 22mg of PM6 and Y6-BO-4F in chlorobenzene at 1:1 ratio and spin-coated onto different HTL at the speed of 2000 rpm for 30 s. The as-spun film was

then annealed at 80 °C for 10 min. Afterward, PFN-Br was spin-coated onto the BHJ layer at the speed of 5000 rpm for 30s. Finally, a 100-nm thick aluminum (Al) counter electrode was deposited by thermal evaporation.

### 3.2.3 Characterization

UV–vis spectra were recorded using Shimadzu UV 2550 in the wavelength range 250 nm to 900 nm. Thickness of NiO films were measured using Elli-Se-UaM8, Micro Electro Mechanical Systems (MEMS) Ellipsometer at ambient atmosphere. The energy level of different NiO films were obtained from UPS using AXIS-NOVA and Ultra DLD with He I (21.2 eV) as photon source. XPS spectra were measured using Electron Spectroscopy for Chemical Analysis (ESCA). Binding energies were referenced to the C-C bond of the C 1s region at 284.5 eV. XRD patterns were characterized by an X-ray diffractometer (Brucker D8-Advance). AFM images were measured using NX-10 (Park Systems) and analysis area was 5  $\mu\text{m} \times 5 \mu\text{m}$ . The current density–voltage ( $J$ – $V$ ) characteristics of the solar cells were measured using a Keithley 4200 source measurement unit. The solar cell performances were characterized under AM 1.5 G condition with an illumination intensity of 100 mW  $\text{cm}^{-2}$ , as generated using an Oriel Sol3A solar simulator (Oriel model 94023A). The  $J$ – $V$  curves of all the devices were measured by masking the active area using a shadow mask with an area of 0.05  $\text{cm}^2$  under ambient atmosphere. Encapsulation of devices was done by simple glass (15 mm  $\times$  10 mm) encapsulation using UV resin XNR 5570 as the adhesive layer with 10 minutes of UV 365 nm illumination to dry the resin.

### 3.3 Results and discussion

**Figure 3-1a and b** present molecular structure and dipole moment of hydroquinone sulfonic acid potassium (HSA-K) and sodium (HSA-Na) salts. According to density functional theory (DFT) calculation using Gaussian B3LYP 6-31G(d), both HSA-K salt and HSA-Na salt demonstrated permanent dipole moment of 9.76 D and 8.28 D respectively.

For NiO, it is previously reported that electrical properties of NiO vary depending on the fabrication condition of NiO.<sup>[18]</sup> As shown in **Figure 3-2 and Table 3-1**, we have utilized 0.05 M NiO solution of which was optimized for the PCE of our NFA based OSCs. Furthermore, in order to clarify the essential role of HTM, we have also compared OSC devices without HTM (bare indium tin oxide, ITO) and OSC devices with NiO as HTM.

For NiO with salts, we have optimized NiO solutions by adding different volume of HSA-K and HSA-Na salts into NiO solution. Detail conditions are explained in the experimental section. For simplicity, NiO with HSA-K salt and NiO with HSA-Na salt are abbreviated as NiO:HSA-K and NiO:HSA-Na respectively.

As shown in **Figure 3-3a**, we measured ultraviolet-visible (UV-vis) transmittance spectra of different NiO films. NiO:HSA-K and NiO:HSA-Na films do not show any parasitic absorption compared to NiO film and exhibited high transmittance over 95% from 350 to 900 nm range. In addition, using Tauc plot method, all NiO films exhibited wide optical bandgaps ( $E_g$ ) of 4.46 eV (Figure 3-3b). These optical properties of NiO films are favorable to minimize absorption losses and effectively block electron injection from the active layer.

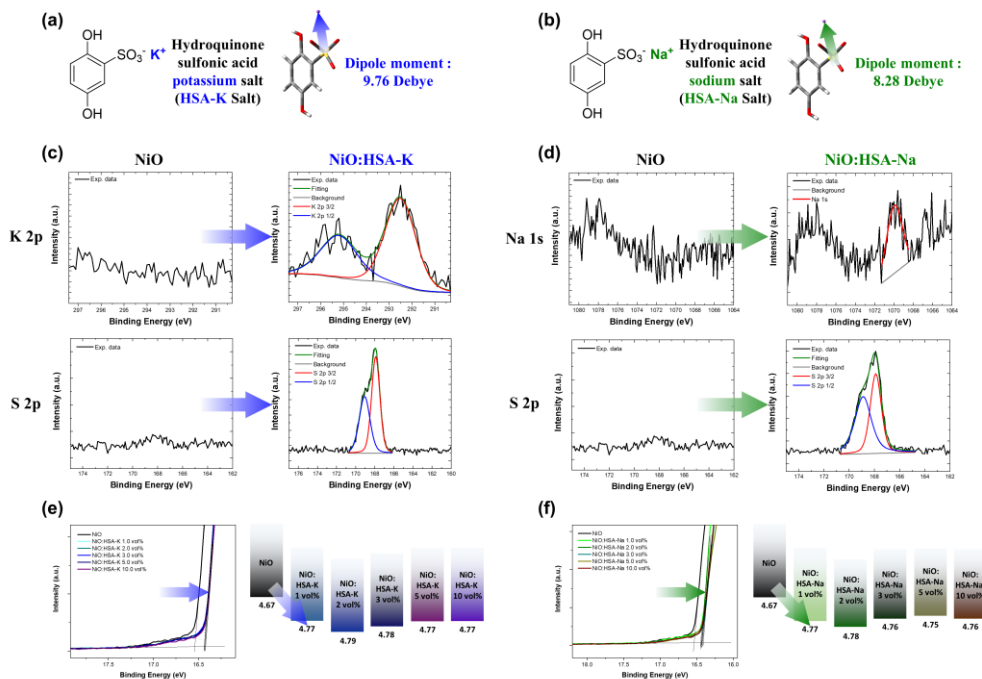


**Figure 3-1.** Molecular structure and dipole moment of a) hydroquinone sulfonic acid potassium (HSA-K) salt and b) hydroquinone sulfonic acid sodium (HSA-Na) salt calculated by DFT calculation using Gaussian B3LYP 6-31G(d). X-ray photoelectron spectroscopy spectra of c) NiO and NiO:HSA-K for K 2p and S 2p orbital, d) NiO and NiO:HSA-Na for Na 1s and S 2p orbital. Ultraviolet photoelectron spectroscopy (UPS) spectra in the cutoff energy regions and their respective work function for NiO films with different amount of e) HSA-K salt and f) HSA-Na salt.

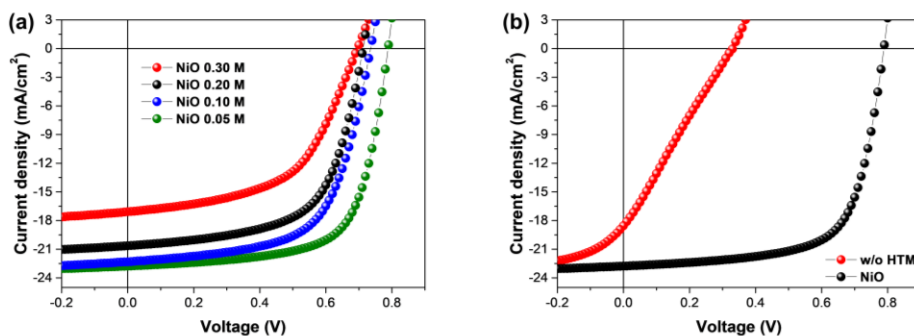


**Figure 3-2.** a)  $J$ - $V$  curves of PM6:Y6-BO-4F OSC devices based on different NiO solutions. b)  $J$ - $V$  curves of PM6:Y6-BO-4F OSC devices without HTM (bare ITO) and with NiO as HTM.

HTM	$V_{oc}$ [V]	$J_{sc}$ [ $\text{mA cm}^{-2}$ ]	FF	PCE
w/o HTM	0.33	18.55	0.24	1.50
NiO 0.30 M	0.69	17.08	0.53	6.24
NiO 0.20 M	0.71	20.64	0.62	9.08
NiO 0.10 M	0.73	21.93	0.63	10.35
NiO 0.05 M	0.79	22.77	0.68	12.19

**Table 3-1.** Photovoltaic parameters of PM6:Y6-BO-4F OSC devices based on different HTM conditions.

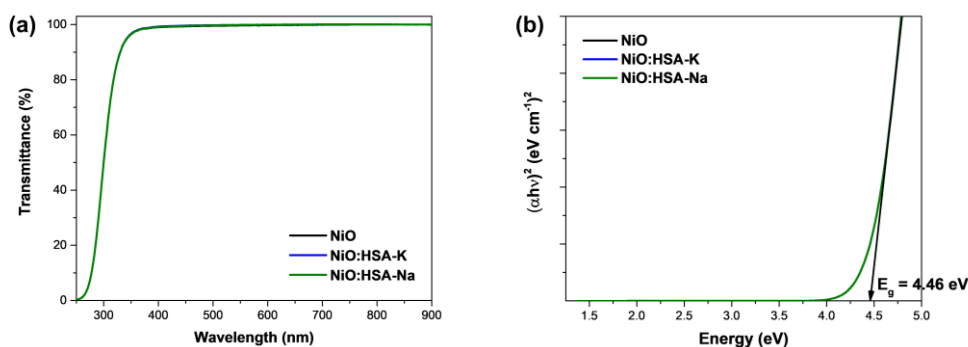


**Figure 3-3.** a) Ultraviolet-visible transmittance spectra of different NiO films from 250 to 900 nm. b) Tauc plots of different NiO thin films to determine optical bandgap.



The morphology and thickness of NiO films were studied using atomic force microscopy (AFM) and spectroscopic ellipsometry. As shown in **Figure 3-4**, NiO films on top of ITO demonstrated very uniform and smooth film coverage. All NiO films of  $\sim 2$  nm thickness on ITO substrate showed root mean square (RMS) roughness no larger than that of bare ITO (1.49 nm).<sup>[19]</sup> NiO:HSA-K (1.41 nm) and NiO:HSA-Na (1.21 nm) films exhibited marginally smaller RMS roughness than NiO (1.42 nm). In order to acquire more accurate thickness of NiO films, we spin coated NiO films on top of perfectly flat SiO<sub>2</sub> substrate and utilized spectroscopic ellipsometry method to optically measure the thickness of NiO films. As shown in **Table 3-2**, both NiO:HSA-K and NiO:HSA-Na films exhibited very small thickness of 1.58 nm and 1.50 nm respectively, which were slightly thinner than NiO (1.61 nm) film. The smooth morphology and small roughness of NiO films are advantageous for formation of active layer on top. Furthermore, the extremely thin NiO films are suitable for effective charge tunneling to occur.<sup>[13a]</sup>

The crystallinity of NiO films was investigated using grazing-incidence X-ray diffraction (GI-XRD) experiments. As shown in **Figure 3-5**, all NiO films exhibited three characteristic peaks at 37.7°, 41.8° and 62.2° for 2 theta values which correspond to (111), (200), and (220) planes of cubic octahedral NiO (bunsenite, NaCl type structure).<sup>[20]</sup> This indicates evident formation of NiO films for all three types of NiO.

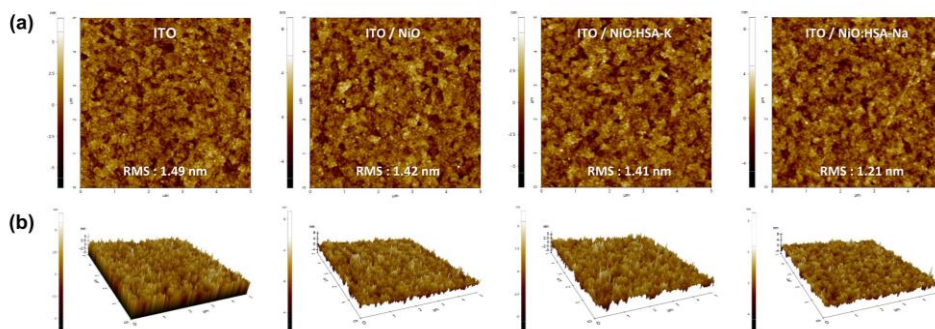


**Figure 3-4.** a) AFM height images of ITO, ITO/NiO, ITO/NiO:HSA-K and ITO/NiO:HSA-Na. b) 3D AFM images.

HTM	Thickness [nm]	Error sigma
NiO	1.61	0.0224
NiO:HSA-K	1.58	0.0216
NiO:HSA-Na	1.50	0.0212

**Table 3-2.** Thickness of different NiO films on top of SiO<sub>2</sub> substrate using spectroscopic ellipsometry measurements.

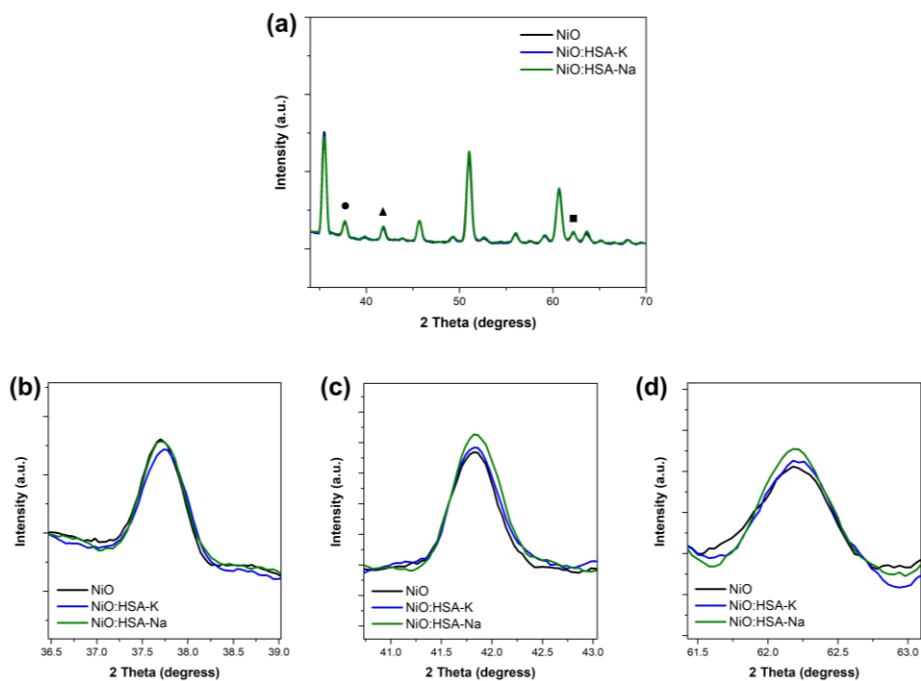


**Figure 3-5.** Grazing-angle X-ray diffraction (GI-XRD) patterns of different NiO films. a) Full XRD patterns and magnified XRD patterns that belongs to b) ●: (111) plane peak, c) ▲: (200) plane peak and d) ■: (220) plane peak.

Then, in order to verify addition of these salts in NiO, we examined the surface composition of NiO films using X-ray photoelectron spectroscopy (XPS). As shown in Figure 3-1c and 1d, clear signals of K 2p and S 2p were detected at corresponding binding energies for NiO:HSA-K. Furthermore, noticeable peaks of Na 1s and S 2p were observed for NiO:HSA-Na. In contrast, no characteristic peaks of K, Na and S were detected in the XPS spectra of NiO film. This confirms the existence of HSA based salt elements in the modified NiO films.<sup>[21]</sup>

The effect of these salts on electrical properties and energy band structure of NiO films were studied using ultraviolet photoelectron spectroscopy (UPS) analysis. The WF was calculated by subtracting the secondary energy cutoffs from the excitation energy (Helium, He: 21.2 eV) ( $E_f = h\nu (21.2 \text{ eV}) - E_{cutoff}$ ). The addition of HSA based salts into NiO allowed effective control and modulation of NiO WF (Figure 1e and 1f). Depending on the amount of salt added, the WF of pristine NiO (4.67 eV) showed different extent of WF shift. NiO with 1 vol% addition of HSA-K and HSA-Na salt both exhibited WF at 4.77 eV with 0.10 eV increase in WF. As shown in **Figure 3-6**, we obtained the largest WF shift of  $0.11 \pm 0.01$  eV at 2 vol% of salt addition for NiO:HSA-K and NiO:HSA-Na, demonstrating deepest WF of 4.79 eV and 4.78 eV respectively. These WF shifts can be attributed to the formation of surface dipole at the very thin surface of NiO layer which originates from the quantum tunneling mechanism.<sup>[22]</sup> NiO:HSA-K and NiO:HSA-Na with 3 vol% or larger volume of salt addition showed saturation in WF increase which can be due to the inherent insulating properties of salt.<sup>[13a, 15a, 23]</sup> These results clearly demonstrate effective energy level modification by the use of HSA based salts in NiO.

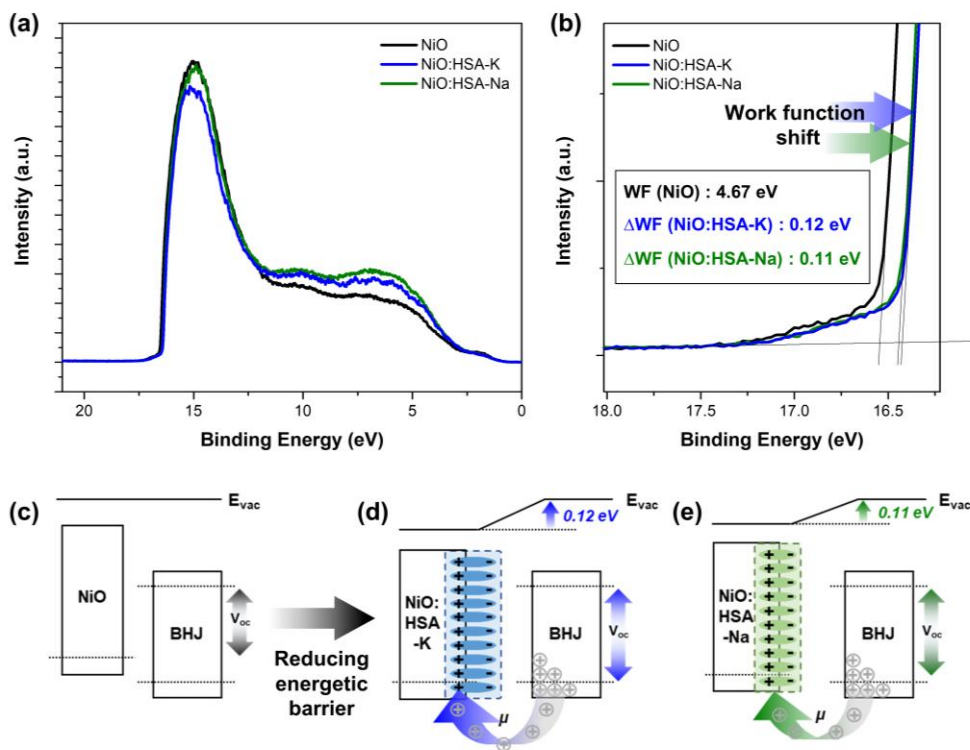


**Figure 3-6.** a) Full UPS spectra and b) UPS spectra in the cutoff ( $E_{cutoff}$ ) energy regions for NiO films. Schematic energy level diagram of c) vacuum level for NiO and vacuum level shift induced by the dipole formation at the surface of NiO using d) HSA-K, and e) HSA-Na.

We fabricated OSCs using simple device configuration of ITO/NiO/BHJ/PFN-Br/Al as shown in **Figure 3-7a and 3b**. We used the most commonly used and high performing donor polymer and NFA pair, PM6 and Y6-BO-4F as the representative BHJ material for NFA based OSCs. In order to examine the effects of HSA based salts and their dipole moment on the surface of NiO, we first fabricated NiO / salt bi-layer structure and tested their performance. We spin-coated different concentration of salt solution on top of NiO layer. As shown in **Figure 3-8 and Table 3-4**, we were able to obtain evident performance enhancement. Compared to the performance of pristine NiO based OSCs with 12.19% ( 0.79 V / 22.77 mA cm<sup>-2</sup> / 0.68 ), spin-coating 1.0 mM concentration of HSA-K and HSA-Na solution above NiO HTL demonstrated the greatest increase in PCE with 14.20% ( 0.85 V / 22.84 mA cm<sup>-2</sup> / 0.73 ) and 14.07% ( 0.85 V / 22.28 mA cm<sup>-2</sup> / 0.74 ) respectively. A clear enhancement in  $V_{oc}$  and FF contributed to the increment in performance.

Furthermore, in order to simplify the fabrication process which is critical for commercialization of photovoltaics, we tried optimization of NiO with addition of HSA based salts into NiO solution. Owing to the extremely thin thickness of NiO films and evident WF shift observed by the addition of salts, we expected sufficient dipoles to be generated at the surface of NiO and effective tunneling to occur in a single layer. As shown in **Figure 3-9 and Table 3-5**, we added different volume ratio of HSA-K and HSA-Na salt into NiO solution and measured their performance. As a result, similar to the changes acquired with bi-layer structure, OSCs demonstrated improvement of performance mainly due to  $V_{oc}$  and FF changes.

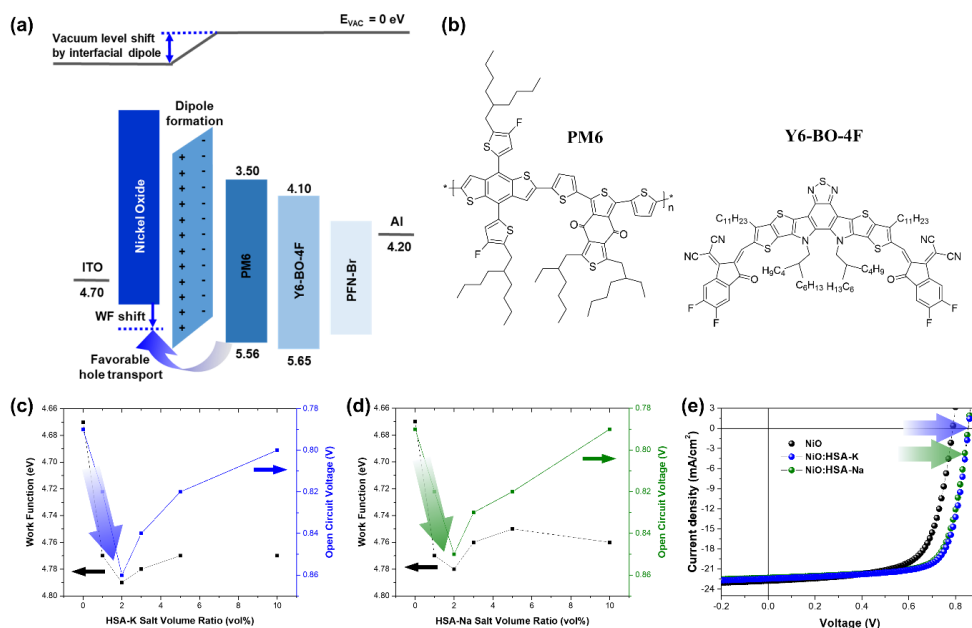


**Figure 3-7.** a) Device configuration and its energy diagram used in this study. b) Molecular structure of PM6 and Y6-BO-4F. Variation of work function and open-circuit voltage depending on the volume ratio of c) HSA-K and d) HSA-Na in NiO. e) *J*-*V* curves of optimized OSC devices with different NiO.

HTM	$V_{oc}$ [V]	$J_{sc}$ [ $\text{mA cm}^{-2}$ ]	FF	PCE
NiO	0.79	22.77	0.68	12.19
NiO:HSA-K	0.86	22.46	0.73	14.19
NiO:HSA-Na	0.85	22.31	0.74	13.94
PEDOT:PSS	0.85	22.53	0.72	13.73

**Table 3-3.** Photovoltaic parameters of optimized OSCs using different HTMs.

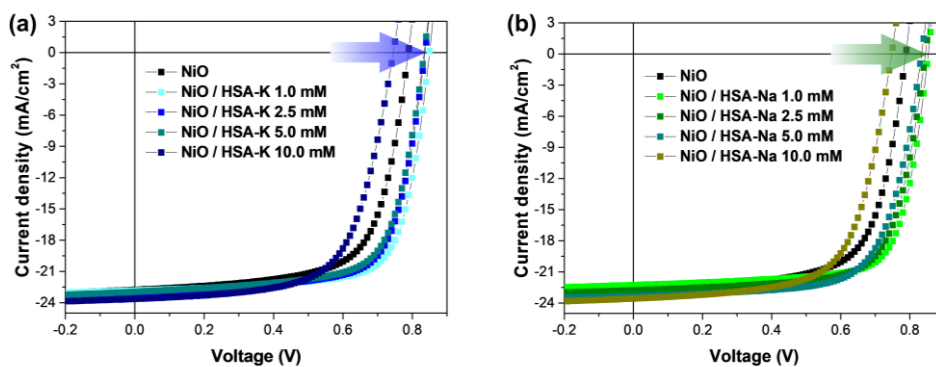


**Figure 3-8.** *J*-*V* curves of PM6:Y6-BO-4F OSC devices using a) NiO / HSA-K and b) NiO / HSA-Na. HSA based salts were tested from 1.0 ~ 10.0 mM concentration.

HTM	$V_{oc}$ [V]	$J_{sc}$ [mA cm <sup>-2</sup> ]	FF	PCE
NiO	0.79	22.77	0.68	12.19
NiO / HSA-K 1.0 mM	0.85	22.84	0.73	14.20
NiO / HSA-K 2.5 mM	0.84	23.05	0.71	13.69
NiO / HSA-K 5.0 mM	0.83	22.96	0.71	13.44
NiO / HSA-K 10.0 mM	0.74	23.63	0.65	11.45
NiO / HSA-Na 1.0 mM	0.85	22.28	0.74	14.07
NiO / HSA-Na 2.5 mM	0.84	22.77	0.71	13.67
NiO / HSA-Na 5.0 mM	0.83	23.32	0.70	13.48
NiO / HSA-Na 10.0 mM	0.75	23.57	0.66	11.61

**Table 3-4.** Photovoltaic parameters of PM6:Y6-BO-4F OSC devices using NiO / HSA based salts.



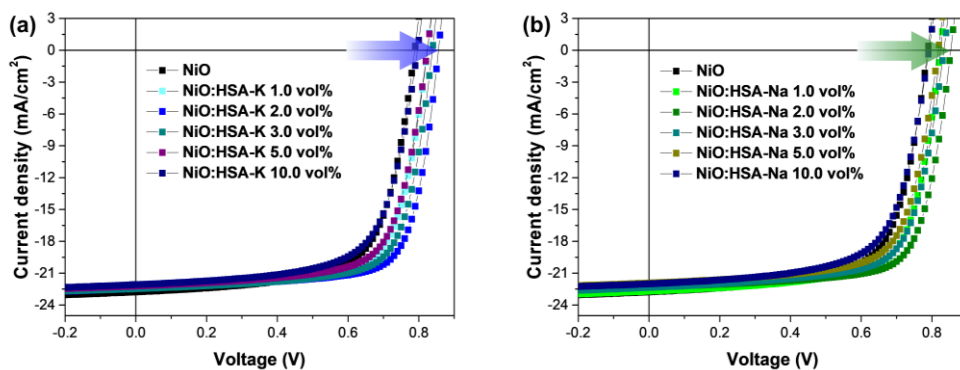


**Figure 3-9.**  $J$ - $V$  curves of PM6:Y6-BO-4F OSC devices based on NiO with different volume ratio of a) HSA-K and b) HSA-Na salt.

HTM	$V_{oc}$ [V]	$J_{sc}$ [ $\text{mA cm}^{-2}$ ]	FF	PCE
NiO	0.79	22.77	0.68	12.19
NiO:HSA-K 1.0 vol%	0.82	22.33	0.72	13.10
NiO:HSA-K 2.0 vol%	0.86	22.46	0.73	14.19
NiO:HSA-K 3.0 vol%	0.84	22.47	0.72	13.63
NiO:HSA-K 5.0 vol%	0.82	22.21	0.71	12.88
NiO:HSA-K 10.0 vol%	0.80	22.07	0.67	11.85
NiO:HSA-Na 1.0 vol%	0.82	22.71	0.71	13.21
NiO:HSA-Na 2.0 vol%	0.85	22.31	0.74	13.94
NiO:HSA-Na 3.0 vol%	0.83	22.35	0.71	13.18
NiO:HSA-Na 5.0 vol%	0.82	21.93	0.70	12.55
NiO:HSA-Na 10.0 vol%	0.79	22.02	0.67	11.64

**Table 3-5.** Photovoltaic parameters of PM6:Y6-BO-4F OSCs based on NiO with different volume ratio of HSA-K and HSA-Na salt.

Notably, we plotted the change of  $V_{oc}$  and WF depending on the volume ratio of HSA-K and HSA-Na added in NiO. As can be seen in Figure 3-3c and 3d, the transition trends of  $V_{oc}$  and WF were very similar. Both the  $V_{oc}$  and WF showed largest increment at 2 vol% of salt addition and exhibited saturation afterwards. As mentioned previously in the UPS section, the saturation of  $V_{oc}$  and WF increase at higher concentration are due to the innate insulating properties of salt which can hinder hole transport or cause hole accumulation. This explains that the performance improvement of OSCs is primarily due to the energy level changes in NiO generated by the HSA based salts and also validates the effectiveness of our approach in using salt to modify NiO.

Optimized performance at 2 vol% ratio for NiO:HSA-K and NiO:HSA-Na demonstrated high PCE of 14.19% ( 0.86 V / 22.46 mA cm<sup>-2</sup> / 0.73 ) and 13.94% ( 0.85 V / 22.31 mA cm<sup>-2</sup> / 0.74 ) respectively (Figure 3-7e and **Table 3-3**). This outperformed that of NiO based OSCs with especially large increase in  $V_{oc}$  (  $0.06 \pm 0.01$  V ) and FF (  $0.05 \pm 0.01$  ). The noticeable reduction of  $V_{oc}$  loss and FF improvement at 2 vol% addition can be attributed to the dipole induced WF adjustment of NiO which alleviated the energetic barrier and facilitated efficient hole transport between BHJ and HTL. Furthermore, as shown in **Figure 3-10**, the champion device based on NiO with HSA salt addition is comparable to that of PEDOT:PSS based OSCs which showed 13.73% ( 0.85 V / 22.53 mA cm<sup>-2</sup> / 0.72 ). To the best of our knowledge, this is also one of the high NFA OSCs based on simple solution processed NiO with high performance over 14% PCE.

In order to study hole transporting ability of different NiO films, we fabricated hole-only devices with configuration of ITO/NiO/Au. As shown in **Figure 3-11**, both

NiO:HSA-K and NiO:HSA-Na demonstrated sharper slope and higher current density than NiO at the same voltage. This implies enhanced hole transport capability for NiO:HSA-K and NiO:HSA-Na, which is in agreement with the observed photovoltaic performances.<sup>[24]</sup>

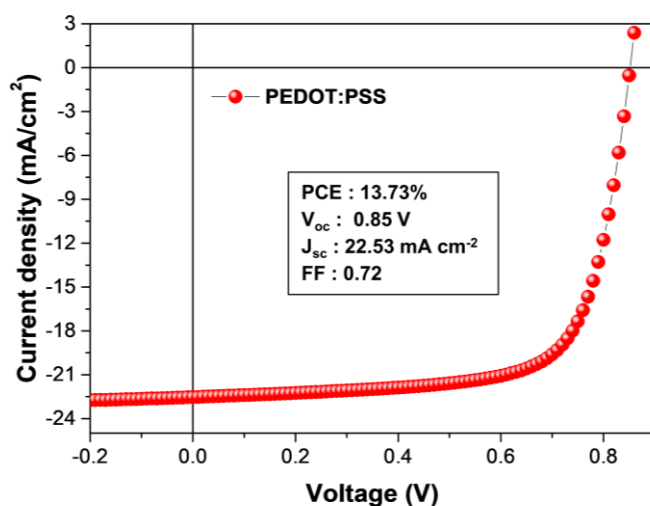


**Figure 3-10.**  $J$ - $V$  curve of PM6:Y6-BO-4F OSC device based on PEDOT:PSS.

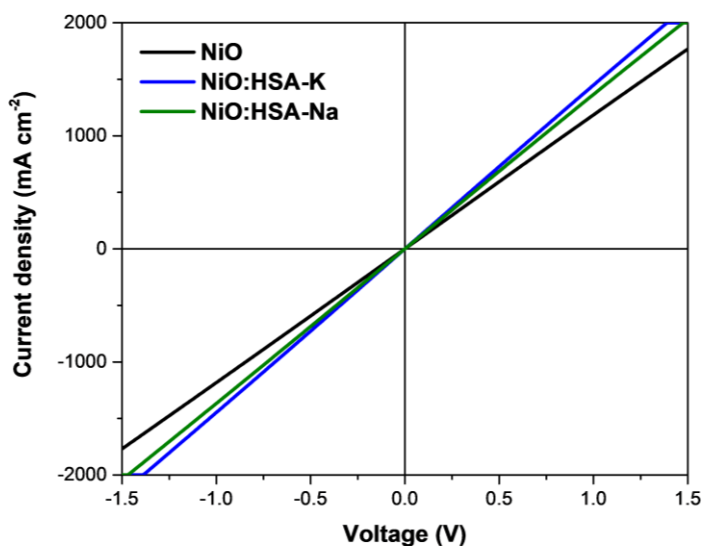


**Figure 3-11.**  $J$ - $V$  curves of hole only devices based on different NiO. The device structure is as follow: ITO/NiO/Au.

Moreover, we examined ambient stability of the fabricated devices in order to investigate the effect of salts on device stability. As shown in **Figure 3-12**, OSC devices with different HTM were encapsulated and kept in ambient atmosphere at relative humidity (RH) of  $40 \pm 5\%$  for 1200 hours. As a result, all NiO based OSC devices demonstrated higher stability compared to PEDOT:PSS based OSC devices which only maintained 25.3% of its initial PCE after 1200 hours. This is due to the acidic and hygroscopic nature of PEDOT:PSS and also relatively more stable nature of oxide materials.<sup>[8]</sup> NiO:HSA-K and NiO:HSA-Na exhibited similar level of stability compared to NiO (46.6%) by maintaining 47.3% and 46.4% of its initial PCE after 1200 hours. The addition of HSA based salts in NiO did not degrade device stability and demonstrated higher ambient stability compared to PEDOT:PSS based devices.

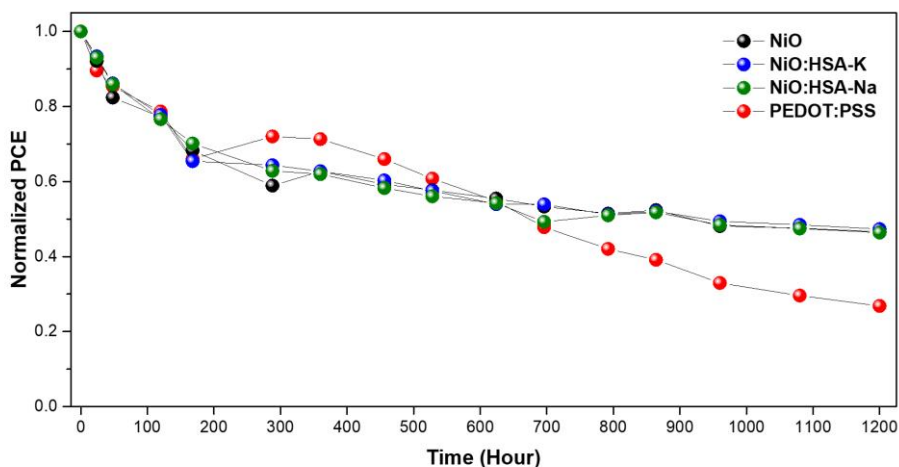


**Figure 3-12.** Air stability of encapsulated OSC devices based on different HTMs.

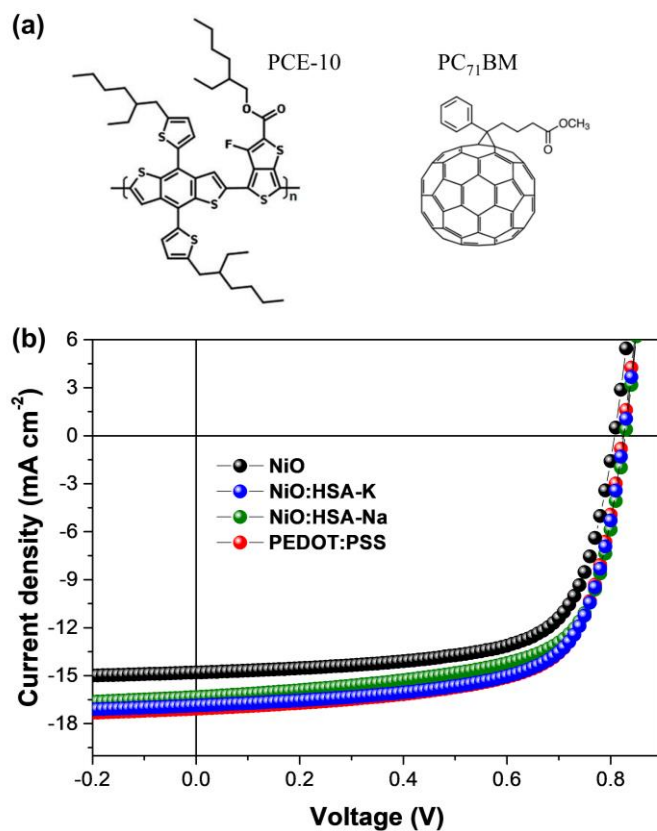


**Figure 3-13.** a) Molecular structure of PCE-10 and PC<sub>71</sub>BM. b) *J-V* curves of optimized fullerene based OSC devices made of ITO/HTM/PCE-10:PC<sub>71</sub>BM/PFN-Br/Al with different HTMs.

HTM	V <sub>oc</sub> [V]	J <sub>sc</sub> [mA cm <sup>-2</sup> ]	FF	PCE
NiO	0.81	15.90	0.68	8.76
NiO:HSA-K	0.83	16.87	0.68	9.53
NiO:HSA-Na	0.82	16.33	0.67	9.07
PEDOT:PSS	0.82	17.07	0.68	9.56

**Table 3-6.** Photovoltaic parameters of PCE-10:PC<sub>71</sub>BM OSCs based on different HTMs.

In addition, we also adopted our strategy on fullerene based OSCs and examined the efficacy of our method. We chose commonly used PC<sub>71</sub>BM as the representative fullerene based acceptor and PCE-10 as the donor polymer. As shown in **Figure 3-13 and Table 3-6**, similar to the improvement we observed in NFA based OSCs, NiO with HSA salts exhibited enhanced performance compared to NiO, and also showed comparable PCE to that of PEDOT:PSS. From these results, we can certify that, our novel strategy of using NiO with HSA based salts is successful in both non-fullerene and fullerene based OSCs by enhancing hole transport between the BHJ and HTL through energy level modification.

### 3.4 Conclusion and outlook

In conclusion, organic small molecule salts with dipole moment have been used successfully to increase the WF of NiO. OSC devices based on NiO with HSA salt modification demonstrated PCE improvement from 12.19% to 14.19% through evident  $V_{oc}$  increase from 0.79 V to 0.86 V. The enhanced performance results from the formation of dipole at the surface of NiO which alleviated energy barrier and facilitated effective hole transport between the active layer and HTL. Through this study, we were able to realize highly efficient and stable NFA OSCs based on NiO HTM for the first time and we hope this study contribute to further development of inorganic HTM.

### 3.5 Bibliography

- [1] a) C. J. Brabec, N. S. Sariciftci, J. C. Hummelen, *Adv. Funct. Mater.* **2001**, *11*, 15;  
b) G. Yu, J. Gao, J. C. Hummelen, F. Wudl, A. J. Heeger, *Science* **1995**, *270*, 1789;  
c) K. M. Coakley, M. D. McGehee, *Chemistry of Materials* **2004**, *16*, 4533; d) C. J. Brabec, *Sol. Energy Mater. Sol. Cells* **2004**, *83*, 273; e) J. Y. Kim, K. Lee, N. E. Coates, D. Moses, T.-Q. Nguyen, M. Dante, A. J. Heeger, *Science* **2007**, *317*, 222.
- [2] a) Y. Cui, Y. Xu, H. Yao, P. Bi, L. Hong, J. Zhang, Y. Zu, T. Zhang, J. Qin, J. Ren, Z. Chen, C. He, X. Hao, Z. Wei, J. Hou, *Adv. Mater.* **2021**, *33*, 2102420; b) Y. Cai, Y. Li, R. Wang, H. Wu, Z. Chen, J. Zhang, Z. Ma, X. Hao, Y. Zhao, C. Zhang, F. Huang, Y. Sun, *Adv. Mater.* **2021**, *33*, 2101733; c) C. Li, J. Zhou, J. Song, J. Xu, H. Zhang, X. Zhang, J. Guo, L. Zhu, D. Wei, G. Han, J. Min, Y. Zhang, Z. Xie, Y. Yi, H. Yan, F. Gao, F. Liu, Y. Sun, *Nat. Energy* **2021**, *6*, 605; d) M. Zhang, L. Zhu, G. Zhou, T. Hao, C. Qiu, Z. Zhao, Q. Hu, B. W. Larson, H. Zhu, Z. Ma, Z. Tang, W. Feng, Y. Zhang, T. P. Russell, F. Liu, *Nature Commun.* **2021**, *12*, 309.
- [3] W. Liu, X. Xu, J. Yuan, M. Leclerc, Y. Zou, Y. Li, *ACS Energy Letters* **2021**, *6*, 598.
- [4] a) Y. Lin, J. Wang, Z.-G. Zhang, H. Bai, Y. Li, D. Zhu, X. Zhan, *Adv. Mater.* **2015**, *27*, 1170; b) A. Armin, W. Li, O. J. Sandberg, Z. Xiao, L. Ding, J. Nelson, D. Neher, K. Vandewal, S. Shoaee, T. Wang, H. Ade, T. Heumüller, C. Brabec, P. Meredith, *Adv. Energy Mater.* **2021**, *11*, 2003570.
- [5] a) J. Yuan, Y. Zhang, L. Zhou, G. Zhang, H.-L. Yip, T.-K. Lau, X. Lu, C. Zhu, H. Peng, P. A. Johnson, M. Leclerc, Y. Cao, J. Ulanski, Y. Li, Y. Zou, *Joule* **2019**, *3*, 1140; b) L. Zhu, M. Zhang, W. Zhong, S. Leng, G. Zhou, Y. Zou, X. Su, H. Ding, P. Gu, F. Liu, Y. Zhang, *Energy Environ. Sci.* **2021**, *14*, 4341.

- [6] a) H.-L. Yip, A. K. Y. Jen, *Energy Environ. Sci.* **2012**, *5*, 5994; b) R. Po, C. Carbonera, A. Bernardi, N. Camaioni, *Energy Environ. Sci.* **2011**, *4*, 285; c) L.-M. Chen, Z. Xu, Z. Hong, Y. Yang, *J. Mater. Chem.* **2010**, *20*, 2575; d) R. Sorrentino, E. Kozma, S. Luzzati, R. Po, *Energy Environ. Sci.* **2021**, *14*, 180.
- [7] Y. Lin, Y. Firdaus, F. H. Isikgor, M. I. Nugraha, E. Yengel, G. T. Harrison, R. Hallani, A. El-Labban, H. Faber, C. Ma, X. Zheng, A. Subbiah, C. T. Howells, O. M. Bakr, I. McCulloch, S. D. Wolf, L. Tsetseris, T. D. Anthopoulos, *ACS Energy Letters* **2020**, *5*, 2935.
- [8] a) B. Ecker, J. C. Nolasco, J. Pallarés, L. F. Marsal, J. Posdorfer, J. Parisi, E. von Hauff, *Adv. Funct. Mater.* **2011**, *21*, 2705; b) M. P. d. Jong, L. J. v. IJzendoorn, M. J. A. d. Voigt, *Appl. Phys. Lett.* **2000**, *77*, 2255.
- [9] a) K. X. Steirer, P. F. Ndione, N. E. Widjonarko, M. T. Lloyd, J. Meyer, E. L. Ratcliff, A. Kahn, N. R. Armstrong, C. J. Curtis, D. S. Ginley, J. J. Berry, D. C. Olson, *Adv. Energy Mater.* **2011**, *1*, 813; b) W. Xu, Y. Liu, X. Huang, L. Jiang, Q. Li, X. Hu, F. Huang, X. Gong, Y. Cao, *J. Mater. Chem. C* **2016**, *4*, 1953; c) M. Qiu, D. Zhu, X. Bao, J. Wang, X. Wang, R. Yang, *J. Mater. Chem. A* **2016**, *4*, 894; d) S. Murase, Y. Yang, *Adv. Mater.* **2012**, *24*, 2459; e) J. R. Manders, S.-W. Tsang, M. J. Hartel, T.-H. Lai, S. Chen, C. M. Amb, J. R. Reynolds, F. So, *Adv. Funct. Mater.* **2013**, *23*, 2993.
- [10] Q. Kang, B. Yang, Y. Xu, B. Xu, J. Hou, *Adv. Mater.* **2018**, *30*, 1801718.
- [11] a) P. Fu, T. Yao, P. Wang, Q. Yang, Y. Ni, X. Guo, C. Li, *Org. Electron.* **2021**, *93*, 106139; b) R. Alkarsifi, Y. A. Avalos-Quiroz, P. Perkhun, X. Liu, M. Fahlman, A. K. Bharwal, C. M. Ruiz, D. Duché, J.-J. Simon, C. Videlot-Ackermann, O. Margeat, J. Ackermann, *Mater. Chem. Front.* **2021**, *5*, 418.



- [12] a) H. N. Tran, S. Park, F. T. A. Wibowo, N. V. Krishna, J. H. Kang, J. H. Seo, H. Nguyen-Phu, S.-Y. Jang, S. Cho, *Advanced Science* **2020**, *7*, 2002395; b) H. N. Tran, H. Lee, C. B. Park, N. V. Krishna, F. T. A. Wibowo, S.-Y. Jang, J. Y. Kim, S. Cho, *Adv. Mater. Interfaces* **2022**, *9*, 2201274.
- [13] a) H. Liu, Z.-X. Liu, S. Wang, J. Huang, H. Ju, Q. Chen, J. Yu, H. Chen, C.-Z. Li, *Adv. Energy Mater.* **2019**, *9*, 1900887; b) B.-H. Jiang, P.-H. Chan, Y.-W. Su, H.-L. Hsu, R.-J. Jeng, C.-P. Chen, *Org. Electron.* **2020**, *87*, 105944.
- [14] Q. Chen, C. Wang, Y. Li, L. Chen, *J. Am. Chem. Soc.* **2020**, *142*, 18281.
- [15] a) C. V. Hoven, A. Garcia, G. C. Bazan, T.-Q. Nguyen, *Adv. Mater.* **2008**, *20*, 3793; b) J. Deng, B. Huang, W. Li, L. Zhang, S. Y. Jeong, S. Huang, S. Zhang, F. Wu, X. Xu, G. Zou, H. Y. Woo, Y. Chen, L. Chen, *Angewandte Chemie International Edition* **2022**, *61*, e202202177; c) C. J. Takacs, Y. Sun, G. C. Welch, L. A. Perez, X. Liu, W. Wen, G. C. Bazan, A. J. Heeger, *J. Am. Chem. Soc.* **2012**, *134*, 16597; d) J.-H. Lee, B. H. Lee, S. Y. Jeong, S. B. Park, G. Kim, S. H. Lee, K. Lee, *Adv. Energy Mater.* **2015**, *5*, 1501292.
- [16] a) R. Peng, T. Yan, J. Chen, S. Yang, Z. Ge, M. Wang, *Advanced Electronic Materials* **2020**, *6*, 1901245; b) X. Wen, A. Nowak-Król, O. Nagler, F. Kraus, N. Zhu, N. Zheng, M. Müller, D. Schmidt, Z. Xie, F. Würthner, *Angewandte Chemie International Edition* **2019**, *58*, 13051.
- [17] S. Park, D. W. Kim, S. Y. Park, *Adv. Funct. Mater.* **2022**, *32*, 2200437.
- [18] a) K. X. Steirer, J. P. Chesin, N. E. Widjonarko, J. J. Berry, A. Miedaner, D. S. Ginley, D. C. Olson, *Org. Electron.* **2010**, *11*, 1414; b) M. T. Greiner, M. G. Helander, Z.-B. Wang, W.-M. Tang, Z.-H. Lu, *J. Phys. Chem. C* **2010**, *114*, 19777; c) F. Jiang, W. C. H. Choy, X. Li, D. Zhang, J. Cheng, *Adv. Mater.* **2015**, *27*, 2930.

- [19] a) Z. Saki, K. Sveinbjörnsson, G. Boschloo, N. Taghavinia, *ChemPhysChem* **2019**, *20*, 3322; b) U. Kwon, B.-G. Kim, D. C. Nguyen, J.-H. Park, N. Y. Ha, S.-J. Kim, S. H. Ko, S. Lee, D. Lee, H. J. Park, *Sci. Rep.* **2016**, *6*, 30759.
- [20] Z. Zhu, Y. Bai, T. Zhang, Z. Liu, X. Long, Z. Wei, Z. Wang, L. Zhang, J. Wang, F. Yan, S. Yang, *Angew. Chem.* **2014**, *126*, 12779.
- [21] B. Ge, H. W. Qiao, Z. Q. Lin, Z. R. Zhou, A. P. Chen, S. Yang, Y. Hou, H. G. Yang, *Sol. RRL* **2019**, *3*, 1900192.
- [22] J. G. Simmons, *Journal of Applied Physics* **1964**, *35*, 2655.
- [23] a) J.-H. Lee, J. Kim, G. Kim, D. Shin, S. Y. Jeong, J. Lee, S. Hong, J. W. Choi, C.-L. Lee, H. Kim, Y. Yi, K. Lee, *Energy Environ. Sci.* **2018**, *11*, 1742; b) A. Vilan, J. Ghabboun, D. Cahen, *The Journal of Physical Chemistry B* **2003**, *107*, 6360.
- [24] W. Chen, F.-Z. Liu, X.-Y. Feng, A. B. Djurišić, W. K. Chan, Z.-B. He, *Adv. Energy Mater.* **2017**, *7*, 1700722.

## 국 문 초 록 (Korean Abstract)

에너지는 21세기의 가장 중요한 이슈 중 하나다. 기후 변화를 저지하고 기후 위기를 예방하기 위해서는 태양광 등의 신재생에너지에 대한 수요 증가가 불가피하다. 현재 상용화된 태양전지의 대부분은 실리콘 기반의 태양전지이지만 페로브스카이트 (Perovskite) 태양전지, 유기태양전지 등 차세대 태양전지에 대한 연구개발이 활발히 이루어지고 있다. 이러한 광전 소자의 성능은 광흡수 물질뿐만 아니라 전하를 각각의 전극으로 선택적으로 수송하는 전하 수송 물질에 의해서도 좌우된다. 혁신적인 소재 및 기술의 개발로 인해 이러한 차세대 태양 전지의 광전 변환 효율이 최근 급격히 상승하면서 기존 실리콘 태양 전지와 어깨를 나란히 할 수 있게 되었다.

본 연구는 기존의 정공 전달 물질로 사용되어 온 PEDOT:PSS 의 성능 및 안정성의 한계점을 극복하고자 니켈 산화물 (Nickel oxide) 을 고성능 광전 소자의 정공 전달 물질로 개발하고 응용하는 데에 관한 연구이다. 염 기반의 스테빌라이저 (stabilizer) 를 활용하여 소자의 안정성과 성능을 모두 향상시키는 전략과 태양전지의 정공 전달 특성을 향상시키기 위해 새로운 쌍극자 보유 첨가제를 도입하였다.

2장에서는 니켈 산화물에 들어가는 스테빌라이저에 대한 연구와 새로운 중성 암모늄 (Ammonium) 기반의 스테빌라이저를 활용하여 소자의 안정성과 효율을 높였다. 스테빌라이저의 대한 연구와 다양한 스테빌

라이저를 도입함에 따라 니켈 산화물의 morphology 와 광전자 특성이 달라지는 것을 확인 할 수 있었다. 정공 전달 물질로 염 스테빌라이저를 포함한 니켈 산화물은 개선된 정공 전달 및 페로브스카이트 층과의 더 강력한 interaction 을 나타내며 향상된 대기 안정성을 보여주었다. 이 새로운 니켈 산화물을 기반으로 매우 안정적이고 효율적인 MAPbI<sub>3</sub> 기반의 페로브스카이트 태양전지를 성공적으로 제작하였다.

3장에서는 기존에 개발된 니켈 산화물에 쌍극자를 띄는 첨가제를 활용하여 효과적인 에너지 준위 변화를 유도하고 소자의 전하 전달 능력을 개선시켰다. 쌍극자 모멘트를 갖는 HSA(Hydroquinone sulfonic acid) 기반의 염은 무기 니켈 산화물 정공 전달 물질과 유기 벌크 이종접합 (bulkheterojunction) 물질 층 사이의 에너지 장벽을 극복하기 위해 첨가제로 활용하였다. 표면 쌍극자의 형성과 전하 터널링은 BHJ 층에서 니켈 산화물로의 정공 전달 특성을 향상시켰습니다. 이 개선된 니켈 산화물을 기반으로 하는 유기 태양전지는 뚜렷한 개방 회로 전압 ( $V_{oc}$ ) 의 증진을 보여주며 이로 인해 금속 산화물 정공 전달 물질을 기반으로 하는 고성능 유기 태양전지를 성공적으로 제작하였다.

**주요어:** 광전자 소자, 정공 전달 물질, 니켈 산화물, 아모니움 솔트 스테빌라이저, 쌍극자를 활용한 에너지 준위 변화

**학 번:** 2017-28672

## List of Publications

1. S. Baik<sup>†</sup>, D. W. Kim<sup>†</sup>, H. Kang, S. H. Hong, **S. Park**, B. An\* and S. Y. Park\*,  
ITIC derivative acceptors for ternary organic solar cells: fine-tuning of  
absorption bands, LUMO energy levels, and cascade charge transfer,  
*Sustainable Energy Fuels*, **2022**, 6, 110-120
2. **S. Park**, D. W. Kim, S. Y. Park\*, Improved Stability and Efficiency of Inverted  
Perovskite Solar Cell by Employing Nickel Oxide Hole Transporting Material  
Containing Ammonium Salt Stabilizer, *Advanced Functional Materials*, **2022**,  
32, 2200437
3. D. W. Kim, M. Choi, W. S. Yoon, S. H. Hong, **S. Park**, J. E. Kwon, S. Y. Park\*,  
Dopant-free donor–acceptor type semi-crystalline polymeric hole transporting  
material for superdurable perovskite solar cells, *Journal of Materials Chemistry  
A*, **2022**, 10, 12187-12195
4. **S. Park**, D. W. Kim, S. Y. Park\*, Highly Efficient Non-Fullerene Organic Solar  
Cells with Nickel Oxide Hole Transporting Layer: Employing Dipole Induced  
Energy Level Modification, *Energy Technology*, **2022**, 2201191
5. M. Choi<sup>†</sup>, **S. Park**<sup>†</sup>, S. Kim, D. W. Kim, S. I. Kim, W. S. Yoon, S. Y. Park\*,  
Multi-Functional NTD based Small Molecule for Both Photovoltaics and  
Transistor Application, (*in preparation*)

## List of Presentations

1. **S. Park**, D. W. Kim, S. Y. Park\*, “Strategic Modification of Nickel Oxide Hole Transport Layer via Chemical Additives for High Performance Perovskite Solar Cell”, ISOPE 2019, Seoul, Korea, 2019.08

## List of Patents

1. 박수영, **박성진**, 김동원, “금속산화물 정공전달층을 구비한 태양전지”, 대한민국 (출원번호 10-2021-0089518 / 현재 심사 중)